Acta Pharmaceutica Sinica B 2024;14(9):4028−4044

Chinese Pharmaceutical Association
Institute of Materia Medica, Chinese Academy of Medical Sciences

Acta Pharmaceutica Sinica B

www.elsevier.com/locate/apsb
www.sciencedirect.com

ORIGINAL ARTICLE

Identification of novel small-molecule inhibitors of SARS-CoV-2 by chemical genetics

Chris Chun-Yiu Chan [a,†], Qian Guo [a,†], Jasper Fuk-Woo Chan [a,b,c,d,†], Kaiming Tang [a,†], Jian-Piao Cai [a,†], Kenn Ka-Heng Chik [a,c], Yixin Huang [e], Mei Dai [f], Bo Qin [f], Chon Phin Ong [e], Allen Wing-Ho Chu [a,c], Wan-Mui Chan [a], Jonathan Daniel Ip [a], Lei Wen [a,c], Jessica Oi-Ling Tsang [a,c], Tong-Yun Wang [a], Yubin Xie [a], Zhenzhi Qin [a], Jianli Cao [a,c], Zi-Wei Ye [e], Hin Chu [a,b,c], Kelvin Kai-Wang To [a,b,c], Xing-Yi Ge [g], Tao Ni [e], Dong-Yan Jin [c,e], Sheng Cui [f], Kwok-Yung Yuen [a,b,c,d], Shuofeng Yuan [a,b,c,*]

[a]*State Key Laboratory of Emerging Infectious Diseases, Carol Yu Centre for Infection, Department of Microbiology, School of Clinical Medicine, Li Ka Shing Faculty of Medicine, the University of Hong Kong, Pokfulam, Hong Kong SAR 999077, China*
[b]*Department of Infectious Diseases and Microbiology, the University of Hong Kong-Shenzhen Hospital, Shenzhen 518000, China*
[c]*Centre for Virology, Vaccinology and Therapeutics, Hong Kong Science and Technology Park, Hong Kong SAR 999077, China*
[d]*Academician Workstation of Hainan Province, Hainan Medical University-the University of Hong Kong Joint Laboratory of Tropical Infectious Diseases, Haikou 571100, China*
[e]*School of Biomedical Sciences, Li Ka Shing Faculty of Medicine, the University of Hong Kong, Pokfulam, Hong Kong SAR 999077, China*
[f]*NHC Key Laboratory of Systems Biology of Pathogens, Institute of Pathogen Biology Chinese Academy of Medical Sciences & Peking Union Medical College, Beijing 100730, China*
[g]*College of Biology, Hunan Provincial Key Laboratory of Medical Virology, Hunan University, Changsha 410082, China*

Received 5 December 2023; received in revised form 24 April 2024; accepted 16 May 2024

*Corresponding author.
E-mail address: yuansf@hku.hk (Shuofeng Yuan).
[†]These authors made equal contributions to this work.
Peer review under the responsibility of Chinese Pharmaceutical Association and Institute of Materia Medica, Chinese Academy of Medical Sciences.

https://doi.org/10.1016/j.apsb.2024.05.026

KEY WORDS

SARS-CoV-2;
High throughput screening;
Broad-spectrum antiviral treatment;
3CLpro inhibitor;
Allosteric-site inhibitor;
Animal models;
Chemical genetics;
Reverse genetics

Abstract There are only eight approved small molecule antiviral drugs for treating COVID-19. Among them, four are nucleotide analogues (remdesivir, JT001, molnupiravir, and azvudine), while the other four are protease inhibitors (nirmatrelvir, ensitrelvir, leritrelvir, and simnotrelvir-ritonavir). Antiviral resistance, unfavourable drug−drug interaction, and toxicity have been reported in previous studies. Thus there is a dearth of new treatment options for SARS-CoV-2. In this work, a three-tier cell-based screening was employed to identify novel compounds with anti-SARS-CoV-2 activity. One compound, designated **172**, demonstrated broad-spectrum antiviral activity against multiple human pathogenic coronaviruses and different SARS-CoV-2 variants of concern. Mechanistic studies validated by reverse genetics showed that compound **172** inhibits the 3-chymotrypsin-like protease (3CLpro) by binding to an allosteric site and reduces 3CLpro dimerization. A drug synergistic checkerboard assay demonstrated that compound **172** can achieve drug synergy with nirmatrelvir *in vitro*. *In vivo* studies confirmed the antiviral activity of compound **172** in both Golden Syrian Hamsters and K18 humanized ACE2 mice. Overall, this study identified an alternative druggable site on the SARS-CoV-2 3CLpro, proposed a potential combination therapy with nirmatrelvir to reduce the risk of antiviral resistance and shed light on the development of allosteric protease inhibitors for treating a range of coronavirus diseases.

1. Introduction

In the past 20 years, the human society has encountered three significant spillovers of novel coronaviruses: SARS-CoV, MERS-CoV, and SARS-CoV-2[1−3]. Among these outbreaks, the COVID-19 pandemic caused by SARS-CoV-2 has resulted in millions of cases and fatalities, and caused a severe impact on the global economy. At the dawn of COVID-19 outbreak, patients typically exhibited symptoms such as cough, congestion, fatigue, fever, breathing difficulties, and ground-glass opacity found in lung CT scans[4−7]. Some patients also experienced diarrhea, confusion, abnormal liver, and renal functions[4,6,7]. However, as the pandemic evolved, COVID-19 has gradually become an upper respiratory tract infection in most cases and symptoms are often mild[8]. Although the world is moving towards a post-COVID phase, it is crucial to be prepared for the emergence of a new variant of SARS-CoV-2 or another zoonotic spillover of coronaviruses from wild reservoirs. One of the crucial measures to control emerging coronavirus outbreaks is to develop effective antivirals with broad-spectrum activity. Currently, there are only three major druggable protein targets in SARS-CoV-2: Spike protein, 3CL-protease (3CLpro), and RNA-dependent RNA polymerase (RdRp)[9−11]. Most monoclonal antibodies initially developed for the treatment of COVID-19 by targeting the Spike protein have failed, due to the emergence of the Omicron variant[12]. There are eight approved small molecule antiviral drugs, yet they are either conventional RdRp or 3CLpro inhibitors[10,13−15]. Four of them (Remdesivir, JT001, Molnupiravir, and Azvudine) are nucleotide analogues[16−19], which could be detrimental to the dividing cells[20,21]. Four of them are 3CLpro inhibitors (Nirmatrelvir/ritonavir, Ensitrelvir, Leritrelvir, and Simnotrelvir/Ritonavir)[10,22−24]. Nirmatrelvir/ritonavir (Paxlovid) is a covalent protease inhibitor, while Ensitrelvir is a non-covalent inhibitor that binds to the substrate-binding pocket of 3CLpro[10,22]. Despite the potent antiviral activity of these drugs, none of them were designed for SARS-CoV-2 specifically and resistance has been reported in some *in vitro* studies[25−28]. Therefore, it is essential to continue the search for novel antivirals. Given the complex life cycle of SARS-CoV-2 which involves multiple steps, there are potentially new antiviral pathways that remain unexplored. Chemical genetics is one of the approaches to reveal novel antiviral pathways. It is the study of functions of genes by disruption with small chemical molecules[29,30]. Chemical genetics has benefits over traditional genetics in the discovery of novel druggable targets. Traditional reverse genetics often relies on altering gene expression, which may not fully capture the complexity of protein function, such as post-translational modifications or protein interactions[29,30]. Additionally, some proteins are essential for normal cellular function, knocking them out could be detrimental. Chemical genetics can be divided into two categories: forward and reverse chemical genetics[30]. Forward chemical genetics involves studying the phenotypic changes caused by small molecules, which can lead to the discovery of novel drug targets[30]. Reverse chemical genetics, on the other hand, requires a defined cellular target, followed by studying its function using small molecules[30]. This approach can be used to identify new small molecules that can achieve a desired phenotype.

In this study, 50,213 raw compounds from the SMART™ Library were screened from a forward chemical genetics direction, to determine their ability to inhibit cytopathic effect on VeroE6 cells. Secondary screening was then performed on A549-TMPRSS2-ACE2 cells to identify compounds with dose-dependent antiviral activity. The antiviral properties of the screened compounds were validated using plaque reduction assay and MTT cytotoxicity assay. Ultimately, five out of 50,213 compounds were confirmed to have anti-SARS-CoV-2 activity *in vitro*. Among these, 10-(4-methylphenyl)-7-phenyl-6,7,8,10-tetrahydro-5*H*-indeno[1,2-*b*]quinoline-9,11-dione (designated compound **172**), exhibited the highest selectivity index (SI), inhibited several SARS-CoV-2 variants of concern (VOC) and multiple human coronaviruses including MERS-CoV, SARS-CoV, and HCoV-229E. Importantly, compound **172** also demonstrated antiviral activity in both Golden Syrian Hamster and K18-hACE mice models. Interestingly, mechanistic studies revealed that compound **172** targets a novel allosteric site on 3CLpro domain III and interferes with protein dimerization. Additionally, compound **172** can achieve drug synergism with Nirmatrelvir, an active compound in Paxlovid[10,31], at nanomolar concentrations. Altogether, these findings suggest the presence of an alternative antiviral

target on coronavirus 3CLpro and provide insights for the development of allosteric protease inhibitors.

2. Materials and methods

2.1. Chemical reagents

SMART™ Library purchased from ChemDiv (San Diego, CA, USA) contains a total of 50,213 structurally diverse synthetic raw compounds. The whole library is formatted in 167,384-well plates of 10 mmol/Lstock concentration dissolved in DMSO per well. The library is kept at −80 °C for storage. Remdesivir, GC-376 and Nirmatrelvir were purchased from MedChemExpress (NJ, USA). FRET-based protease activity substrate: dabcyl-KTSAVLQSGFRKM-E(Edans)-NH_2 was purchased from Bachem Bioscience (Bubendorf, Switzerland). CellTiter Glo® cell viability assay kit was purchased from Promega USA.

2.2. Cell and virus culture

Multiple cell lines were used in this study: VeroE6, Vero-TMPRSS2, A549-TMPRSS2-ACE2, Huh7, U251, and HK2. VeroE6, U251, Huh7, and HK2 were maintained in DMEM supplemented with 5%−10% fetal bovine serum (FBS) and 1% penicillin/streptomycin (PS). Vero-TMPRSS2 was maintained in 10% FBS DMEM supplemented with 1% PS and 1 mg/mL G-418 for marker selection. A549-TMPRSS2-ACE2 was maintained in 10% FBS DMEM supplemented with 1% PS, 0.5 μg/mL Puromycin, and 300 μg/mL Hygromycin for marker selection. All cell lines were passaged at least once per week.

Several SARS-CoV-2 variants were used in this study: Wild Type (strain HKU-001a) (GenBank: MT230904), strain B.1.1.7 (Alpha) (GenBank: OM212469), strain B.1.617.2 (Delta) (GenBank: OM212471), Omicron BA.1, and Omicron BA.5 (GenBank: OM212472). These variants were isolated from patients with laboratory confirmed COVID-19 in Hong Kong[32]. Virus expansion and propagation were conducted as previously described[32]. The resulting virus stocks were stored at −80 °C. MERS-CoV (EMC/2012) was kindly provided by Ron Fouchier (Erasmus Medical Center, The Netherlands). Archived clinical strains of SARS-CoV-1 (GZ50 strains, GenBank: AY304495), and HCoV-229E were obtained from the Department of Microbiology, the University of Hong Kong. Experiments involving live SARS-CoV-2 virus were performed in the BSL-3 facility located in Block T of Queen Mary Hospital.

2.3. Primary screening of SMART™ library by CellTiter-Glo® assay

VeroE6 cells were dispensed onto 384-well plates at a density of 5000 cells per well using a liquid dispenser. Selected SMART™ stock plates were diluted 20-fold using the Apricot S1 automatic 384 format liquid handling system (Apricot Designs, USA), and 0.5 μL of the diluted stock was added to each well using the same system. A positive control, Remdesivir at 10 μmol/L, was added to column 23. The cells and compounds were co-incubated overnight at 37 °C with 5% CO_2 before being transferred to the BSL-3 facility for infection with SARS-CoV-2 WT strain D614G at a multiplicity of infection (MOI) of 0.01 in 10 μL per well, except for column 1 and 24 which served as mock infections. The final compound concentration was 5 μmol/L. After a 3-day incubation at 37 °C with 5% CO_2, CellTiter Glo® reagent was added to each well, and cell viability was measured using a plate reader located inside the BSL-3 facility. The primary screening was performed in duplicate, and compounds that demonstrated >60% cell viability in both duplicates were selected for secondary screening. The cell viability data was analysed using a self-developed R studio script.

2.4. Secondary screening by RT-qPCR

The day before infection, A549-TMPRSS2-ACE2 cells were seeded onto 96-well plates at a density of 20,000 cells per well. On the following day, the plates were transferred to the BSL-3 facility for infection with SARS-CoV-2 strain D614G at MOI 0.01. After a 1-h adsorption period, the cell supernatant was removed, and the cells were washed once with PBS before being treated with primary hit compounds that had been prepared in advance at concentrations of 20, 5, and 1.25 μmol/L. Following a 2-day incubation period at 37 °C with 5% CO_2, the cell supernatant was collected and lysed using RLT lysis buffer. RNA extraction was performed using the RNeasy kit (Qiagen, Germany) according to the manufacturer's protocol. The extracted RNA was then quantified using the Takara One-Step TB Green® PrimeScript™ RT-QPCR kit II (Takara, Japan) and SARS-CoV-2 RdRp/Hel gene primers as described previously[32]. Primary hit compounds that resulted in more than a 2-log10 viral load reduction in one or more concentrations were considered as secondary hits and would be validated by Plaque Reduction Assay in tertiary screening.

2.5. Plaque reduction assay

Briefly, compounds of interest were prepared in 2× gradient concentrations using 2% FBS/2% PS DMEM and mixed with LMP-agarose at a 1:1 ratio after a 1-h virus adsorption period. The compound-agarose mixture was then overlayed onto cells, and the plates were inverted and placed in a 37 °C/5% CO_2 incubator for 3 days. A solution of 10% formalin in PBS was used to fix the cells, and a 0.25% solution of crystal violet was used to stain the plaques. The GraphPad Prism software was used to compute an IC_{50} value for each compound that demonstrated a reduction in plaque activity without significant cell toxicity.

2.6. MTT cytotoxicity assay

Briefly, cells were seeded onto a 96-well plate at a density of 20,000 cells per well one day before treatment. On the following day, compounds of interest were added to the cells in gradient concentrations and incubated at 37 °C with 5% CO_2 for either 48 or 96 h. After medium removal, 100 μL of 1 × MTT solution in plain DMEM was added to the cells and incubated at 37 °C with 5% CO_2 for 3−4 h. Then, MTT lysis buffer (10% SDS/10 mmol/L HCl) was added to the cells and incubated at room temperature for 3−4 h. Cell viability was measured in absorbance (OD_{595}) using a plate reader (Glomax, Promega).

2.7. SARS-CoV-2 N antigen expression assay

After infecting VeroE6 cells with SARS-CoV-2 for 1 h at a 37 °C/5% CO_2 incubator, the medium was removed and replaced with 1% FBS 1% PS DMEM containing the compound of interest. After 3 days post-infection (dpi), the medium was removed, and the cells were fixed with a 10% formaldehyde solution in PBS for

15 min. Following this, the formaldehyde was removed, and the cells were rinsed briefly with Virkon before being transferred to a BSL-2 laboratory for IF staining. The IF staining process involved adding 0.1% Triton X-100 in PBS to permeabilize the cells. Next, 2% bovine serum albumin (BSA) in PBS was used to incubate the cells for 1 h at room temperature (RT) to reduce non-specific bindings of the primary antibody. Then, an in-house rabbit antiserum against SARS-CoV-2 N protein, diluted at a ratio of 1:200 in 1% BSA in PBS, was added to the cells and incubated at 4 °C overnight. The cells were washed twice with PBS-T (0.05% Tween 20 in PBS) after removing the primary antibody, followed by the addition of Alexa Fluor secondary antibody (ThermoFisher Scientific, USA) at 1:500 dilution and incubation for 1−2 h at RT. The cells were then labeled with 4′,6-diamidino-2-phenylindole (DAPI) nucleic acid stain (ThermoFisher Scientific, USA) to label cell nuclei and mounted with the Diamond Prolong Antifade mountant (ThermoFisher Scientific, USA). Finally, the stained cells were observed under a fluorescent microscope to determine the antigen's intensity.

2.8. Viral load reduction assay by RT-qPCR

Viral load reduction assay was performed by quantitative reverse transcription-polymerase chain reaction (RT-qPCR) with slight modifications from a previously described protocol[33]. RNA was extracted from the culture supernatants of CoV-infected cell lines, as described earlier, using the RNeasy extraction kit (Qiagen, Germany). Reverse transcription was performed using the Transcriptor First Strand cDNA Synthesis Kit from Roche (Basel, Switzerland) with oligodT primers. To determine the virus genome copies, qPCR was performed using the LightCycler 480 SYBR Green I Master Mix from Roche with specific primers. The virus genome copies in the supernatant samples were quantified with a standard using the following specific primers: hCoV-229E_Forward: CTACAGATAGAAAAGTTGCTTT; hCoV-229E_Reverse: GGTCGTTTAGTTGAGAAAAGT; SARS-CoV (-2)_Forward: CGCATACAGTCTTRCAGGCT; SARS-CoV(-2) _Reverse: GTGTGATGTTGAWATGACATGGTC; MERS-CoV_Forward: GGGTGTACCTCTTAATGCCAATTC: MERS-CoV_Reverse: TCTGTCCTGTCTCCGCCAAT.

2.9. Generation and RT-qPCR validation of escape mutant

To investigate the antiviral mechanism of compound **172**, an escape mutant was generated. Vero-TMPRSS2 cells were seeded onto a 12-well plate at a density of 4×10^5 cells per well one day before infection to generate passage 1. On the next day, SARS-CoV-2 WT D614G was inoculated into the cells at MOI 1 in the presence of 5 μmol/L of compound **172** or 0.05% DMSO (control). After 48 h of incubation at 37 °C/5% CO_2, around 50% CPE formation was observed. The supernatant of passage 1 was transferred to a new plate of Vero-TMPRSS2 cells and absorbed for 1 h at 37 °C, and the remaining of passage 1 was stored at −80 °C. After 1 h, the cell medium was replaced with 6 μmol/L of compound **172** or 0.06% DMSO, and the plate was incubated at 37 °C/5% CO_2. This procedure was repeated with decreasing MOI and increasing drug concentration. At passage 6, CPE formation was observed in the presence of 8 μmol/L compound **172**, and it was collected for plaque quantification, escape mutant validation, and Nanopore sequencing.

The escape mutant was validated using the RT-qPCR method. Vero-TMPRSS2 cells were seeded onto a 96-well plate at a density of 20,000 cells per well one day before infection. The cells were then infected with the virus from passage 6 and passage 0 (strain D614G) at MOI 0.01, and treated with compound **172** in gradient concentration after 1 h of virus adsorption. After 48 h post-infection (hpi), the cell supernatant was collected, and RNA was extracted using the RNeasy kit from Qiagen (Germany) following the manufacturer's protocol. The viral RNA copy was measured using the Takara One-Step TB Green® PrimeScriptTM RT-qPCR kit II from Takara (Japan) with SARS-CoV-2 RdRp/Hel gene as mentioned previously.

2.10. Nanopore sequencing of escape mutant

Nanopore sequencing technology (Oxford Nanopore Technologies, UK) was used to perform whole genome sequencing of SARS-CoV-2, as previously described[34]. RNA was extracted from passage 6 using the RNeasy kit (Qiagen, Germany) and then reverse transcribed into cDNA using SuperScript™ IV reverse transcriptase (ThermoFisher Scientific, USA) according to the manufacturer's protocol. PCR was performed using the ARTIC nCoV-2019 V3 Panel (IDT, USA) and Q5® Hot Start High-Fidelity 2X Master Mix (New England Biolabs, USA), as per the manufacturer's protocol. PCR product cleanup was conducted using 1 × Agencourt AMPure XP (Beckman Coulter, USA). End-prep, barcode ligation, and sequencing adaptor ligation were performed according to the PCR tiling of SARS-CoV-2 virus with Native Barcoding Expansion 96 protocol (Version: PTCN_9103_v109_revH_13Jul2020). The library was loaded and sequenced on MinION with R9.4.1 flow cells for 48 h. Nanopore sequencing data were analysed following the Artic Network nCoV-2019 novel coronavirus bioinformatics protocol with minor modifications[35].

2.11. Generation of recombinant mutant virus from Bacterial Artificial Chromosome (BAC)

An infectious molecular clone of SARS-CoV-2 on a Bacterial Artificial Chromosome (BAC) was used. The 3CLpro S301P substitution was introduced into the clone using λ-Red-mediated homologous recombination, as we previously described[36]. Firstly, homologous recombination was carried out to insert a galK expression cassette, which was amplified using 50-bp 3CLpro-flanking homology arms to bind to plasmid pMOD4-galK-G (5′−3′ Forward: GTAGTGCTTTATTAGAAGATGAATTTACAC CTTTTGATGTTGTTAGACAACCTGTTGACAATTAATCATC GGCA; 5′−3′ Reverse: GTGGTGTGTACCCTTGATTGTTCT TTTCACTGCACTTTGGAAAGTAACACTCAGCACTGTCCT GCTCCTT). The galK cassette was introduced into the site of interest by electroporation into competent *E. coli* SW105 strain. Electroporated bacterial cells were plated onto M63 minimal agar supplemented with galactose for 3 days at 32 °C. The galK-bearing clone was isolated and purified, and then subjected to a second round of recombination. Secondly, annealed oligonucleotides bearing the 3CLpro S301P mutation ordered from Integrated DNA Technologies (IDT) were electroporated to substitute the galK cassette (5′−3′ Forward: GTAGTGCTTTATTAGAAGATGAATTTACACCTTTTGATG TTGACAATGCCCAGGTGTTACTTTCCAAAGTGCAGTGA AAAGAACAATCAAGGGTACACACCAC; 5′−3′ Reverse: GTGGTGTGTACCCTTGATTGTTCTTTTCACTGCACTTTGG AAAGTAACACCTGGGCATTGTCTAACAACATCAAAAGGT GTAAATTCATCTTCTAATAAAGCACTAC). The electroporated-

bacterial cells were plated onto M63 minimal agar supplemented with 2-deoxy-galactose to remove the galK-bearing clone. The successful clone was screened using PCR amplification flanking the 3CLpro site of interest, and the point mutation was confirmed through Sanger Sequencing. Purified BAC bearing the 3CLpro S301P mutation was extracted using the PureLink™ HiPure BAC Buffer Kit (ThermoFisher Scientific, USA).

Recombinant virus rescue was performed in Vero-TMRPSS2 cells. 6 μg of BAC was transfected into the cells using Lipofectamine 3000 according to the manufacturer's instructions, and then transferred into a BSL-3 facility. After 6 h, the BAC-containing medium was replaced with serum-free DMEM. The cells were monitored for cytopathic effect over the course of 3 days. Upon confirmation of the cytopathic effect, virus-containing supernatant was clarified and harvested. SARS-CoV-2 3CLpro S301P was further passaged in VeroE6-TMPRSS2 cells, and the viral titers were determined using plaque assay.

2.12. Validation of antiviral resistance recombinant mutant virus

The antiviral resistance phenotype of the recombinant mutant virus was confirmed using three methods: phenotypic observation, RT-qPCR, and plaque reduction assay. Phenotypic validation involved observing CPE formation. Vero-TMRPRSS2 cells were seeded onto a 96-well plate at a density of 20,000 cells/well one day before infection. On the following day, the cells were infected with recombinant WT and 3CLpro S301P mutant viruses at an MOI of 0.01, and the cell medium was replaced with compound **172** in gradient concentration after 1 h of virus adsorption. After 48 hpi, CPE formation was observed under an electronic light microscope, and photos were taken in the BSL-3 facility. Cell supernatant was collected and RNA extraction was performed using the RNeasy kit from (Qiagen, Germany) following the manufacturer's protocol. The SARS-CoV-2 viral RNA of both recombinant WT and mutant viruses was measured by RT-qPCR using the Takara One-Step TB Green® PrimeScript™ RT-qPCR kit II (Takara, Japan), with SARS-CoV-2 RdRp/Hel gene primers as mentioned. Plaque reduction assay was also used to validate the antiviral resistance phenotype of the recombinant mutant virus as previously described.

2.13. Drug synergism checkerboard assay

Compound **172** and Nirmatrelvir were prepared in a gradient of 4 × concentrations, mixed in a checkerboard pattern at a 1:1 ratio, and added to A549-TMPRSS2-ACE2 cells were seeded onto 96-well plates one day before. On the next day, wild type SARS-CoV-2 was then added to the cells at a 1:1 volume ratio with a MOI of 0.1. After 48 h post-infection (hpi), CellTiter Glo® reagent was added to the cells, and cell viability was measured in luminance using a plate reader in a BSL-3 facility. The cell viability was normalized and fitted into a non-linear regression model using GraphPad Prism, and an IC_{50} value was calculated for each compound with the corresponding partner compound concentration. The paired IC_{50} values with the corresponding partner compound concentrations were plotted as a scatterplot for data visualization. The paired values were also fitted into the Loewe's additivity (LA) equation, as Eq. (1):

$$[A]/IC_{50[A]} + [B]/IC_{50[B]} = 1 \quad (1)$$

2.14. Expression and purification of SARS-CoV-2 WT and mutant 3CL-protease

Recombinant SARS-CoV-2 WT 3CLpro and mutant (S301P) using the reference Wuhan-Hu-1 (GenBank ID: YP_009724390.1) were codon-optimized and cloned into pET28b+ for *E. coli* BL21 expression as previously described[37]. A 6 × His tag was added to the N-terminal of each protein construct for Ni-NTA purification. To induce recombinant 3CLpro production, the *E. coli* subculture was grown until reaching an OD_{600} absorbance of 0.6, and then induced with 0.5 mmol/L isopropyl β-D-1-thiogalactopyranoside (IPTG) at 25 °C for 16 h with agitation. After overexpression, the bacterial pellet was collected, lysed with 0.1% Triton X-100 in PBS, and stored at −80 °C overnight. The total proteins were released from the lysate through sonication, followed by centrifugation at 13,000×*g*/4 °C for 30 min. The solution was passed through the Ni-NTA column twice to bind, washed with 500 mL washing buffer (50 mmol/L NaH_2PO_4, 300 mmol/L NaCl, 40 mmol/L imidazole, pH 8.0) at a controlled and steady flow rate, then eluted with 10 mL elution buffer (50 mmol/L NaH_2PO_4, 300 mmol/L NaCl, 250 mmol/L imidazole; pH 8.0) into fractions. The purity of each fraction was analysed by SDS-PAGE followed by Coomassie blue staining. The concentration of the purified 3CLpro was determined using the Bradford Assay.

2.15. Fluorescence-based protease activity assay

A fluorescent-resonance-energy-transfer (FRET)-based protease activity assay was developed to investigate the inhibitory effects of compound **172** on the enzymatic activity of WT and mutant 3CLpro. Compound **172** was prepared in 50× gradient concentration in DMSO, while substrate (dabcyl-KTSAVLQSGFRKM-E(Edans)-NH_2) and 3CLpro (WT or S301P) were prepared in 2× concentration in reaction buffer (50 mmol/L HEPES, 0.1 mg/mL BSA, 5 mmol/L DTT, pH 7.5). 1 μL of 50 × compound **172** was added into 25 μL of 2× 3CLpro and incubated at room temperature for 30 min on a black walled 384-well plate (ThermoFisher Scientific, USA). Then, 25 μL of 2× substrate was added to the mixture. Fluorescence (excitation/emission: 365 nm/500−550 nm) was measured by a plate reader (Glomax, Promega) after 20 min. The initial velocity of fluorophore release was normalized against DMSO control. GC-376 was used as a positive control throughout the experiment.

2.16. Michaelis−Menton inhibitory kinetics assay

A Michaelis−Menton inhibitory kinetic assay was conducted to compare the modes of inhibition between compound **172** and Nirmatrelvir on WT 3CLpro. Compound **172** and Nirmatrelvir were prepared in a 2-fold gradient 100 × concentrations in DMSO, while substrate (dabcyl−KTSAVLQSGFRKM-E(Edans)−NH_2) and WT 3CLpro were prepared in 2 × concentration with reaction buffer (50 mmol/L HEPES, 0.1 mg/mL BSA, 5 mmol/L DTT, pH 7.5). 1 μL of 100× compound **172** or Nirmatrelvir was added to 50 μL of 2× 3CLpro and incubated at room temperature for 30 min on a black walled 96-well plate (ThermoFisher Scientific, USA). Then, 50 μL of 2× substrate was added to each well and incubated

for an additional 20 min, followed by measuring fluorescence (excitation/emission: 365 nm/500−550 nm) using a plate reader (Glomax, Promega). The initial velocity was calculated by dividing the fluorescent intensity by incubation time. The data was fitted into the mixed-model inhibition function to generate alpha values in GraphPad Prism. According to GraphPad Prism, when alpha value equals 1, it represents the ideal non-competitive inhibition[38]. When the alpha is greater than 1, the inhibitor preferentially binds to the free enzyme, and if it is very large, the model approaches competitive inhibition[38]. When alpha is less than 1, the inhibitor preferentially binds to the enzyme−substrate complex, and if it is very small, the model approaches an uncompetitive model[38].

2.17. Surface plasmon resonance (SPR) spectroscopy

To verify the interaction between compound **172** and 3CLpro, a surface plasmon resonance (SPR) experiment was carried out on the Biacore T-200 machine (Cytiva, USA). First, WT or mutant 3CLpro was diluted with acetate buffer (pH 5.0) to reach a concentration of 40 μg/mL or higher and immobilized onto a Series S Sensor Chip CM5 until a response unit of 15,000 RU was achieved. Next, a running buffer containing 5% DMSO in 1× PBS was prepared, and compound **172** and GC-376 were prepared in gradient concentrations, with one concentration duplicated. DMSO was used as a negative control and background. "LMW kinetics" was selected in the Biacore software protocol wizard, and compounds were added onto a 96-well U-bottom plate based on the layout generated in the software. The reaction was started according to the software instructions. After overnight incubation, the SPR results, including the drug−protein response curve and affinity curve were generated.

2.18. Analytical ultracentrifugation (AUC) assay

The sedimentation velocity experiment was carried out using a Beckman Coulter Optima analytical ultracentrifuge (Beckman Coulter, USA), equipped with an An-60 Ti rotor, at a temperature of 20 °C. To examine the dimer-inhibitory effect of **172** against SARS-CoV-2 3CLpro, the 600 μg/mL freshly purified WT 3CLpro was incubated with 20 μmol/L **172** or 0.2% DMSO for at least 2 h on ice before this assay. Then the sample was centrifuged at 40,000 rpm using 12-mm standard double sector centerpieces. A total of 400 scans were taken at 4-min intervals, featuring the data resolution at 10 μm. The detection of monomer or dimer, based on radial position and time, was achieved through absorbance measurements at 280 nm, as well as interference detection. The resulting profiles were analyzed using Sedfit software's continuous distribution model.

2.19. Golden Syrian golden hamster experiment

Golden Syrian hamsters, either male or female, aged between 4 and 6 months, were accommodated in a BSL-3 facility and provided with standard food pellet and water. The hamsters were grouped randomly in groups of 4 ($n = 4$) for antiviral assessment. All experimental protocols were approved by the Animal Ethics Committee at the University of Hong Kong (CULATR), and were conducted according to the standard operating procedures of the BSL-3 animal facilities (reference code CULATR 5370-20). The treatment group hamsters received the first dose of compound **172** (dissolved in 20% SBE-β-CD/0.9% saline at the concentration of 1 mg/kg), while the control group received 5% DMSO in vehicle. Both groups were administered through intraperitoneal (i.p.) injection 3 h before infection. The experiments were not blinded. Each hamster received a nasal inoculation of 1000 PFU of Wild Type SARS-CoV-2 in 50 μL PBS while under i.p. anaesthesia with ketamine (200 mg/kg body weight) and xylazine (10 mg/kg body weight). Five hours after being infected with SARS-CoV-2, the hamsters received the second dose of treatment or DMSO vehicle. In the following 3 days, the hamsters were treated with a daily Q12 regimen of treatment and were monitored for signs of illness and changes in body weight. The same protocol was followed for an *in vivo* drug toxicity experiment, except that the virus was not inoculated. The infected hamsters were euthanized 3 days after virus inoculation for virological and histopathological examination. Their lungs and nasal turbinate were collected for viral RNA detection and plaque quantification. The tissue pathology of infected animals was examined by Hematoxylin and Eosin staining, and immunofluorescence staining, according to an established protocol[37].

2.20. K18-hACE2 mouse survival experiment

Male or female K18-hACE2 transgenic mice, aged between 6 and 8 weeks, were accommodated at the BSL-3 animal facility, and provided with standard food pellet and water. The use of K18-hACE2 transgenic mice has been approved by the CULATR of The University of Hong Kong under Animal Ethics Committee (reference code: 5370-20). On the day of infection, the hACE2 mice were intranasally inoculated with either 200 PFU B.1.1.7, 1 or 10,000 PFU B.1.1.529 sub-lineage BA.5, pre-diluted in 20 μL PBS. Mice were treated with either 50 mg/kg compound **172** in 20% SBE-β-CD/0.9% saline, 200 mg/kg PF-07321332 (Nirmatrelvir) in vehicle or 5% DMSO in vehicle, by i.p. injection daily until sample collection or animal death. The body weight and survival of the mice were monitored on a daily basis. Mice were euthanized at designated timepoints and organ tissues were sampled for virological analyses. The mice's lungs and nasal turbinate were collected for viral RNA detection and plaque quantification[19].

2.21. Molecular docking

The 3D structure of compound **172** was retrieved from the PubChem database[39] with ID 3700821. The high-resolution dimer structure of SARS-CoV-2 main protease (Mpro) was downloaded from the Protein Data Bank (PDB) database[40] with ID 6Y2G. The structure of Mpro bound to Pelitinib was retrieved with PDB ID 7AXM. The charge/protonation state of Mpro protein was assigned with H++ server[41]. Potential ligand-binding pockets of Mpro was probed with Metapocket[42]. Leadfinder v.1804[43] was used to dock compounds against Mpro protein with extra precision mode (-xp). Intermolecular interaction plot was generated by Pymol.

2.22. Molecular dynamics (MD) simulation

The best-scoring binding poses of **172**−Mpro complex was used as the initial conformation and solvated in cubic water box with the TIP3P water model, extending to at least 10 Å from the protein atoms. The ff14SB force field[44] was used to describe the protein, together with general Amber force field (GAFF)[45] parameters for ligands. The simulation was carried out using the Amber17 package[46], long-range electrostatics were treated with the particle

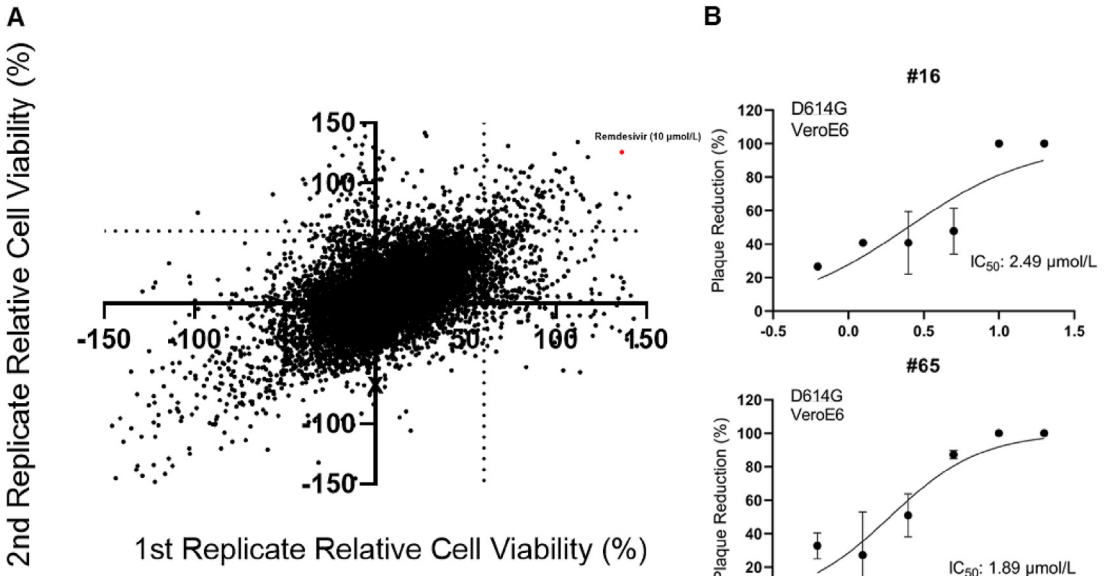

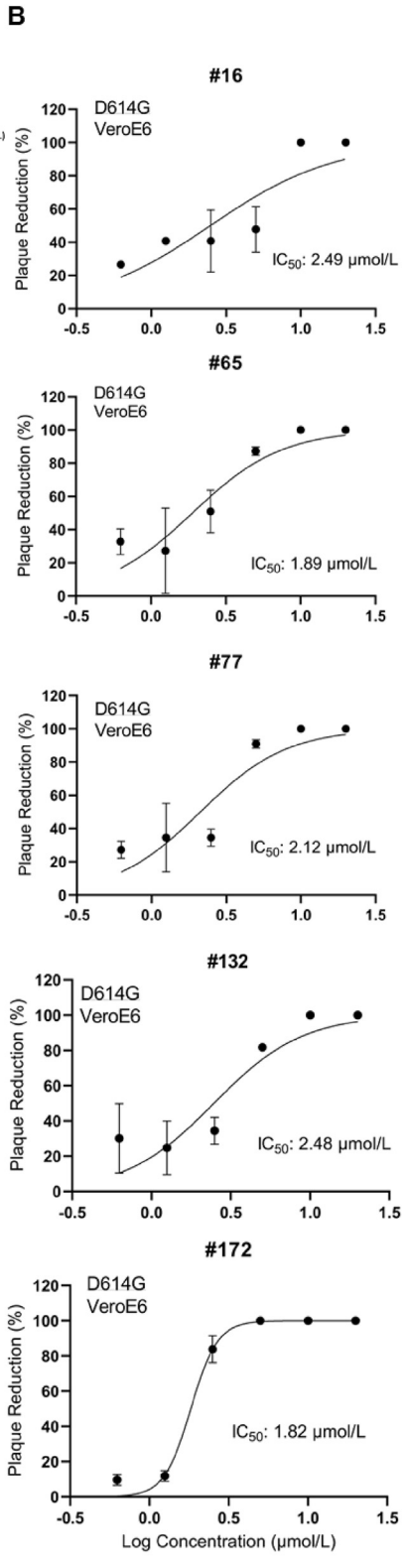

C

Compound number	Chemical structure	VeroE6 CC_{50} (μmol/L)	Plaque Reduction IC_{50} (μmol/L)	Selectivity Index (CC_{50}/IC_{50})
16	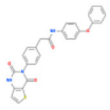	37.67	2.49	15.3
65	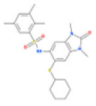	>100	1.89	>52.9
77	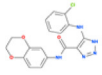	32.05	2.12	15.1
132		>100	2.48	>40.3
172		>100	1.82	>54.9

Figure 1 Phenotype-based high-throughput antiviral screening. (A) Primary screening results using a CPE-inhibition assay. The primary screening cutoff was set as over 60% cell viability in both duplicates. Out of 50,213 compounds, 168 were identified to satisfy this criterion. Mock infection was included to normalize the cell viability (100%). Remdesivir was added at a concentration of 10 μmol/L as positive control (shown in red). (B) Plaque reduction assay results of the five finalized compounds. VeroE6 cells were inoculated with 40 PFU of SARS-CoV-2 D614G virus and subsequently treated with each of the five selected hit compounds, which were diluted from 20 to 1.25 μmol/L in 2-fold intervals. At 72 hpi, the cells were fixed with 10% formalin/PBS and stained with a 0.5% crystal violet solution to visualize the plaques. The IC_{50} value was calculated

mesh Ewald method, while the van der Waals interactions were truncated at a cutoff of 10 Å. After 1 ns of equilibration, three 10 ns production runs were carried out in the NPT ensemble at 300 K. The time step was 2 fs, and snapshots were saved for analysis every 20 ps.

2.23. *Permeability of compound **172** in Caco-2 assay*

Caco-2 cells were seeded onto 0.4 μm pore polycarbonate membranes (PC) in 96-well Corning Insert plates at a density of 3.5×104 cells/cm^2. HBSS with 10.0 mmol/L HEPES at pH 7.40 ± 0.05 as the transport buffer. The compound was subjected to bidirectional testing in triplicate at 2.00 μmol/L. The plate was incubated in a CO_2 incubator with 5% CO_2 at 37.0 °C and saturated humidity for 2 h without shaking. All samples were centrifuged at $3220\times g$ for 10 min after being combined with acetonitrile containing internal standard. Using the peak area ratio of the analyte/internal standard, LC−MS/MS techniques were used to quantify the concentrations of the compound in the beginning solution, donor solution, and recipient solution. Following transportation, lucifer yellow rejection assay was applied to determine the Caco-2 cell monolayer integrity.

For data analysis, permeability (P_{app}), efflux ratio, and percent recovery were calculated using Eqs. (2)−(4):

$$P_{app} = (dCr/dt) \times Vr/(A \times C_0) \quad (2)$$

$$\text{Efflux ratio} = P_{app\ [BA]}/P_{app\ [AB]} \quad (3)$$

$$\text{Solution recovery } (\%) = 100 \times [(Vr \times Cr) + (Vd \times Cd)] / (Vd \times C_0) \quad (4)$$

Reference compounds were analysed in parallel as assay control.

2.24. *Metabolic stability of compound **172** in mouse and human liver microsomes*

Mouse and human liver microsomes were respectively provided by RILD and corning. They were collected from CD-1 mouse or human and prepared in 100 mmol/L potassium phosphate buffer. The reaction was started by the addition of 100 μmol/L compound **172** working solution with or without NADPH co-factor and terminated by adding cold (4 °C) acetonitrile (ACN) containing 250 nmol/L tolbutamide and 250 nmol/L labetalol. Aliquots were sampled at 0, 5, 15, 30, 45, and 60 min for LC−MS/MS analysis.

2.25. *Mouse pharmacokinetics study*

The pharmacokinetic characteristics of compound **172** after a single intraperitoneal dosage of 5 mg/kg on BALB/c mice were investigated. There were three male mice (6−10 weeks) in the experimental group and the dose volume will be determined by the animals' body weight collected on the morning of dosing day. At 0.25, 0.5, 1, 2, 4, 6, 8, and 24 h after dosage, blood samples were obtained from saphenous vein and placed in tubes containing EDTA-K2. After $3200\times g$ of centrifugation at 4 °C for 10 min, plasma samples were quickly frozen over dry ice and kept at −80 °C. Identification of compound **172** in plasma was performed by LC−MS/MS analysis on DG-Triple Quad 6500 plus. Pharmacokinetic parameters were calculated by i.p.-noncompartmental model 200 using Phoenix WinNonlin 8.3.5.

3. Results

3.1. *Phenotype-based high throughput screening*

The phenotypic-based high throughput screening (HTS) was performed in three levels (Supporting Information Fig. S1). First, primary screening was conducted by screening 50,213 synthetic compounds for their CPE inhibition (CPEi) activity against SARS-CoV-2 wildtype (WT) D614G infection in VeroE6 cells. CellTiter Glo® reagent was added to cells to measure cell viability after 72 h-post-infection (hpi). Over 60% cell viability in both duplicates was set as a selection criterion in primary screening. As a result, 168 out of 50,213 compounds were discovered to inhibit over 60% CPE formation in VeroE6 cells at 5 μmol/L (Fig. 1A). Afterwards, the 168 primary hits were moved onto secondary screening using human A549-TMPRSS2-ACE2 cells. Forty out of 168 compounds were found to reduce 2-$\log_{10}$ or higher SARS-CoV-2 viral load using at least one concentration (Supporting Information Fig. S2). Next, 40 secondary screen hits were validated for their anti-SARS-CoV-2 activity by plaque reduction assay. Ultimately, five out of 40 compounds were confirmed to reduce anti-SARS-CoV-2 infectious particles with a 50% effective dose (IC_{50}) at lower μmol/L levels (<5 μmol/L, Fig. 1B) without significant cytotoxicity. These final hits, designated **16**, **65**, **77**, **132**, and **172**, also reduced SARS-CoV-2 N protein expression in VeroE6-TMPRSS2 cells by immunofluorescent (IF) staining (Supporting Information Fig. S3). The greatest reductions in N protein expression were observed in compound **172** (Fig. S3), which is consistent with plaque reduction assay result (Fig. 1B). While the remaining four compounds exhibited a moderate degree of reduction in N antigen expression (Fig. S3). MTT cytotoxicity assay was also conducted to confirm that the antiviral phenotype was not due to drug cytotoxicity (Supporting Information Fig. S4). The selectivity index (SI) of these five compounds was calculated as shown (Fig. 1C). Compounds **16** and **77** have lower SI (15.3 and 15.1, respectively) due to their lower CC_{50} values (37.67 and 35.05, respectively). For compounds **65**, **132**, and **172**, their SI are higher (>52.9, >40.3, and >54.9, respectively) which achieve CC_{50} values higher than 100 μmol/L.

3.2. *Prioritization of the compounds*

Among the five candidates, one of them (compound **172**) exhibits the lowest IC_{50} (1.82 μmol/L) and high CC_{50} (>100 μmol/L), which gives a SI > 54.9 (Fig. 1C). Therefore, we decided to investigate further on its antiviral potency and mechanism. Although

by fitting the number of plaque formations against the logarithmic concentrations of the compounds using a non-linear regression model in GraphPad Prism software. (C) Antiviral profiles of the five selected compounds with their chemical structure, IC_{50} (by plaque reduction assay), CC_{50} (by MTT cytotoxicity assay), and selectivity index (SI) as shown. The highest tested concentration in the MTT cytotoxicity assay was 100 μmol/L due to the maximal water solubility in 1% DMSO.

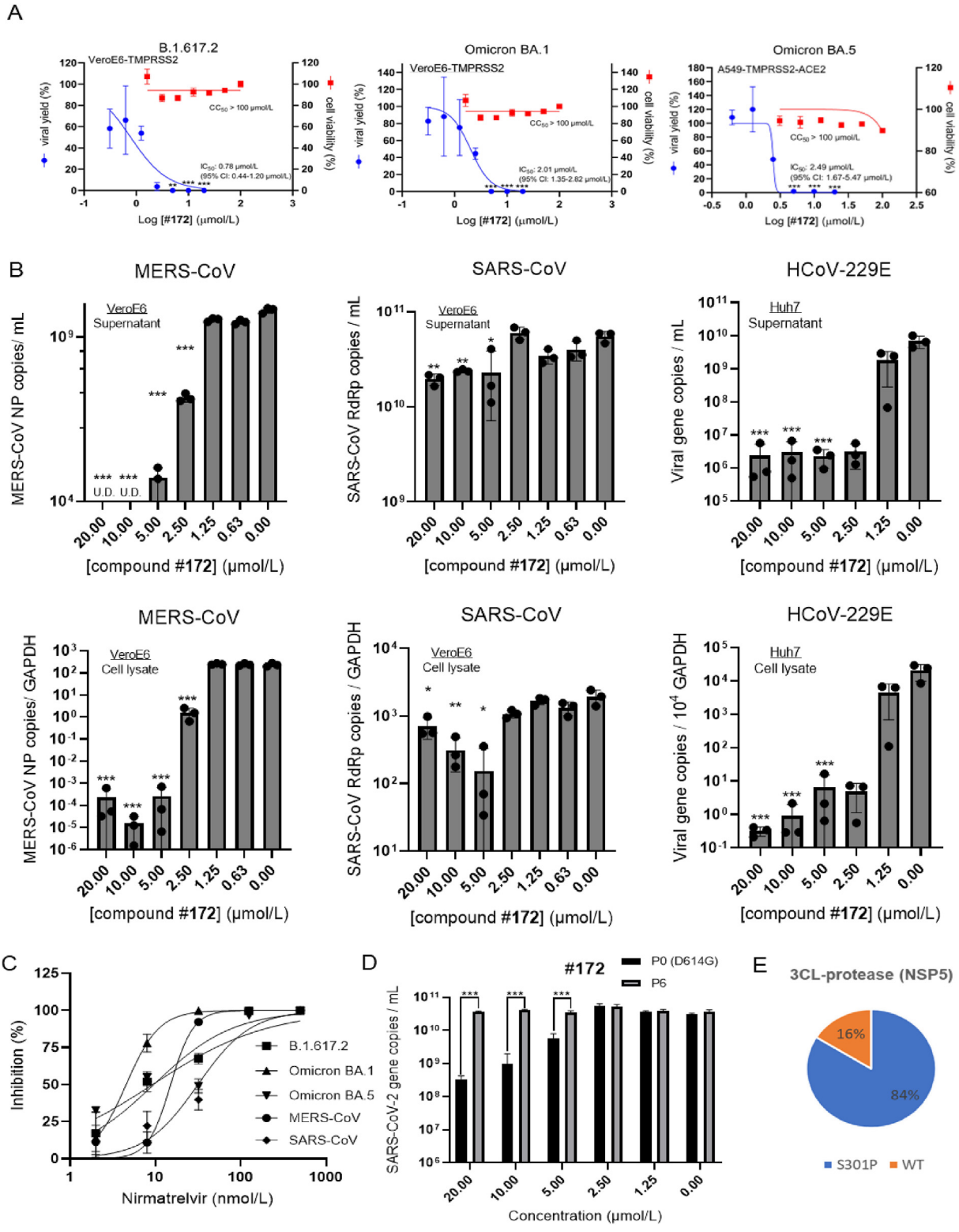

Figure 2 Pan-coronavirus activity and raise of escape mutant of compound **172.** (A) viral load reduction assay conducted against SARS-CoV-2 VOC Delta, Omicron BA.1/BA.5, and co-plotted with cytotoxicity using MTT cytotoxicity assays. The viral yield was expressed as a percentage of DMSO control. Compound **172** was diluted in 2-fold intervals from 20 μmol/L to 0.3125 μmol/L, and the IC_{50} value was calculated by fitting the normalized viral load against the logarithmic concentrations using a non-linear regression model in GraphPad Prism software. MTT cytotoxicity assays were carried out as previously described. (B) VeroE6 or Huh7 cells were infected with MERS-CoV, SARS-CoV, or HCoV-229E at MOI 0.01. After 48 hpi, the supernatant and cell lysate were collected and lysed, and the viral RNA copies were measured using RT-qPCR. (C) Antiviral activity of Nirmatrelvir as a reference control of compound **172**. (D) VeroE6-TMPRSS2 cells were infected either by Passage 0 (D614G virus) or Passage 6 virus at MOI 0.01, followed by treatment with varying concentrations of compound **172**. After 48 h, the supernatant was

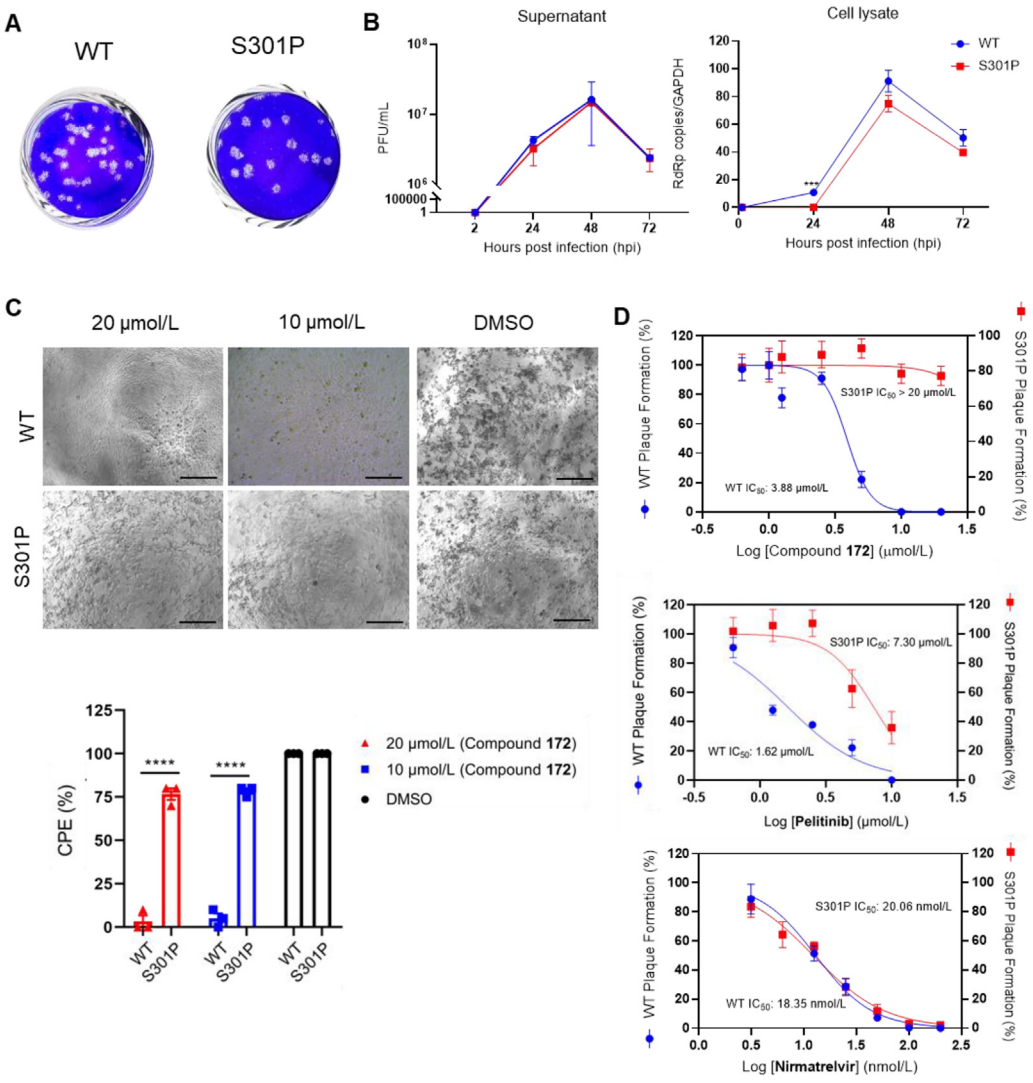

Figure 3 Characterization of compound **172**-resistant S301P recombinant SARS-CoV-2. (A) Plaque morphology of recombinant WT and 3CLpro S301P virus. VeroE6-TMPRSS2 cells were utilized to culture and quantitate 3CLpro S301P virus, which was rescued using VeroE6-TMPRSS2 cells. (B) Replication kinetics of 3CLpro S301P recombinant virus. Both recombinant WT and mutant viruses replicate at comparable rate, 3CLpro S301P showed slight attenuation in growth rate. (C) Microscopic images of recombinant WT and 3CLpro S301P mutant virus in the presence of compound **172** and percentages of CPE of each image. VeroE6-TMPRSS2 was infected with either virus at MOI 0.01 and treated with compound **172** at different concentrations ranging from 20 to 0.625 μmol/L. Representative images of CPE formation were captured at 48 hpi. Scale bar = 100 μm. The experiment was performed in triplicate and repeated twice for confirmation. The CPE severity in each group was scored and compared by two-way ANOVA. (D) Plaque formation assay of recombinant WT and 3CLpro S301P virus under the treatment of compound **172,** Pelitinib, and Nirmatrelvir, respectively. Antiviral IC_{50} of each drug compound against WT and mutant viruses were plotted by GraphPad. Data are presented as mean ± SD. $^{****}P < 0.0001$; $^{***}P < 0.001$.

compound **65** has a comparable SI with **172**, it was not chosen to be studied further because it demonstrated some extent of cytotoxicity in VeroE6 cells at 20 μmol/L using plaque reduction assay, which corresponds to 80% cell viability in MTT assay, yet **172**-treated cells had over 90% cell viability at 100 μmol/L and high tolerability in multiple cell lines (Fig. S4). Interestingly, compound **172** was potent against other variants of concerns (VOC) of SARS-CoV-2, such as B.1.617.2 (Delta), Omicron BA.1 and Omicron BA.5, with micromolar IC_{50}(Fig. 2A). Compound **172** could also inhibit the replication of MERS-CoV, SARS-CoV, and HCoV-229E *in vitro* and in a dose-dependent manner (Fig. 2B). Notably, compound **172** reduced the MERS-CoV supernatant viral RNA level below the RT-

collected and the viral load was measured using RT-qPCR. Statistical analysis for all the assays above were performed by Student's *t*-test: Data are presented as mean ± SD. $^{***}P < 0.001$; $^{**}P < 0.01$; $^{*}P < 0.05$. (E) Nanopore sequencing results. 84% virus population carried S301P point mutation in the 3CLpro. **172** Escape mutant was raised in six passages in VeroE6-TMPRSS2, by reducing MOI and increasing **172** concentrations in each passage, until the CPE inhibition effect of **172** was abolished.

qPCR detection limit at 5 μmol/L or above, and > 5-log10 reduction in the normalized expression of N gene in cell lysate (Fig. 2B). Additionally, more than 3-log10 viral RNA reduction was observed in the supernatant of HCoV-229E infected Huh7 cells and similar results were found in the cell lysate (Fig. 2B). Lastly, compound **172** demonstrated 1-log10 reduction of SARS-CoV viral load in the supernatant and cell lysate (Fig. 2B). As a reference control, Nirmatrelvir shows potent antiviral effects against SRAS-CoV-2 variants and other human coronaviruses with sub-nanomolar IC_{50} values ranging from 4.5 to 32 nmol/L (Fig. 2C). Taken together, compound **172** exhibits pan-coronavirus antiviral activity.

3.3. *Mode of action of compound 172*

To investigate the antiviral mechanism of compound **172**, an escape mutant was generated. After six rounds of passages with increasing compound **172** concentration (Supporting Information Fig. S5A), CPE inhibition by compound **172** was abolished at 8 μmol/L in passage 6. Therefore, passage 6 was collected for plaque quantification and escape mutant validation (Fig. S5A). Interestingly, passage 6 was completely resistant toward compound **172** when compared to passage 0 (WT D614G), as shown by RT-qPCR analysis (Fig. 2D). Moreover, Nanopore sequencing discovered more than 80% virus population in passage 6 carried a single nonsynonymous mutation at the 10,955 genome locus: a T to C nucleotide mutation, which results in the amino acid substitution of serine by proline at the 301th position (S301P) of 3CLpro (Fig. 2E), when compared to that of passage 0. This single point mutation was also verified by traditional Sanger sequencing (Fig. S5B).

To validate the correlation between 3CLpro S301P and compound **172**, a recombinant mutant virus was constructed using bacterial artificial chromosome (BAC) recombineering technology. 3CLpro S301P virus was generated and validated by traditional Sanger sequencing (Fig. S5C). The mutant virus was rescued and passaged successfully in VeroE6-TMPRSS2 cells (Fig. 3A). Replication kinetics of recombinant WT and mutant S301P virus demonstrated comparable growth rate with slight attenuation in the mutant virus (Fig. 3B). As expected, compound **172** demonstrated CPE inhibition phenotype in VeroE6-TMPRSS2 cells infected by recombinant WT virus, whereas the CPEi phenotype was abolished and cell syncytia could be observed under the infection of S301P virus (Fig. 3C). Moreover, plaque formation assay with the treatment of compound **172** resulted in an IC_{50} value of 3.88 μmol/L in recombinant WT, comparable with previous screening results (Fig. 3D). However, when the cells were infected by mutant S301P virus, no plaque reduction phenotype was observed, which indicated antiviral resistance (Fig. 3D). The result also suggests that 3CLpro S301 residue is critical for the antiviral phenotype of compound **172**. To further elucidate the antiviral mechanism of compound **172**, the S301P virus was tested against two "reference compounds" with the clarified mode of action, nirmatrelvir and Pelitinib. Nirmatrelvir is a peptidomimetic inhibitor, the active component of Paxlovid[10]. Interestingly, both recombinant WT and S301P viruses are susceptible to nirmatrelvir, with similar IC_{50} (18.35 and 20.06 nmol/L) *in vitro* (Fig. 3D). This suggests 3CLpro S301P does not confer resistance towards nirmatrelvir and implies the antiviral mechanism of compound **172** is different from nirmatrelvir. On the other hand, Pelitinib is an epidermal growth factor receptor (EGFR) inhibitor[47]. An X-ray crystallography screening study suggested that Pelitinib could interact with an allosteric site of SARS-CoV-2 3CLpro associated with S301, resulting in antiviral activity[48]. Indeed, antiviral IC_{50} of Pelitinib increased from 1.62 μmol/L towards recombinant WT virus to 7.30 μmol/L against the mutant virus (Fig. 3D), which verified the important role of S301 in this proposed allosteric site. Taken together, the result implied that compound **172** is a 3CLpro allosteric inhibitor associated with S301.

To confirm 3CLpro is the antiviral target of compound **172**, WT and S301P 3CLpro were expressed and purified, for fluorescent-resonance-energy-transfer (FRET)—based protease activity assays and surface plasmon resonance (SPR) spectroscopy. Notably, compound **172** exhibited a dose-dependent inhibition of WT 3CLpro cleavage activity *in vitro*, yet was unable to inhibit S301P 3CLpro activity (Fig. 4A). Utilizing SPR spectroscopy, compound **172** was demonstrated to bind with 3CLpro with a dissociation constant (K_d) of 3.65 μmol/L, while a higher K_D was estimated for S301P protein (K_d = 11.9 μmol/L) (Fig. 4B and C). Altogether, our findings confirmed that 3CLpro is the antiviral target of compound **172**.

Moreover, Michaelis−Menton inhibitory kinetics was conducted to compare the mode of inhibition of compound **172** and nirmatrelvir. Notably, the inhibitory constant (K_i) for compound **172** and nirmatrelvir differ greatly: 274.2 and 192.2 nmol/L (Fig. 4D and E), suggesting **172** could be targeting the dimeric interface which is not revealed at native conditions. Importantly, the Alpha values for compound **172** and nirmatrelvir are 1.50 and 0.60 respectively (Fig. 4D and E). This indicates compound **172** is a weak competitive inhibitor while nirmatrelvir is a non-competitive inhibitor under this experimental setup[38]. The results suggest compound **172** inhibits 3CLpro by a different mode of action other than direct catalytic inhibition by nirmatrelvir.

In addition, the analytical ultracentrifugation (AUC) was conducted to explore the effects of **172** on 3CLpro dimerization. Upon mixing 20 μmol/L of compound **172** with WT 3CLpro, there was a significant reduction on 3CLpro dimerization, reducing its contribution by about 10% (Fig. 4F, Supporting Information Fig. S6A). Taken together, compound **172** can induce considerable effects on 3CLpro conformation by disrupting its dimerization.

On the other hand, due to distinct MOAs between compound **172** and nirmatrelvir, it is interesting to investigate the mode of interaction between two compounds. Therefore, a drug synergism checkerboard assay was conducted. Notably, when compound **172** was at nanomolar concentration, **172**-nirmatrelvir synergism could be achieved, as shown by the two green points within the "isobole" (Supporting Information Fig. S7A). Fitting the IC_{50} values of nirmatrelvir with the corresponding compound **172** concentration into the Loewe's additivity (LA) equation also yielded consistent results: when compound **172** was at 312.5 and 156.25 nmol/L, the LA values were smaller than 1 (0.58 and 0.24 respectively) (Fig. 4I). This indicated that **172**-nirmatrelvir drug synergism can be achieved when compound **172** is at nanomolar concentrations.

Based on the identified S301 amino acid residue responsible for compound **172** resistance (Fig. 3), molecular docking predicted that compound **172** binds to a novel allosteric site situated between the two monomers of 3CLpro, which is different from that of Pelitinib[48] (Fig. 4G and H). Specifically, the allosteric site bound by Pelitinib is comprised of Y118, L141, N142, I213, L253, Q256, V297, C300, S301, and G302[48]. However, **172**'s allosteric site was predicted to be surrounded by M6, F8, Y118, N119, S121, S123, L141, I152, D153, F294, R298, Q299, and S301. Human

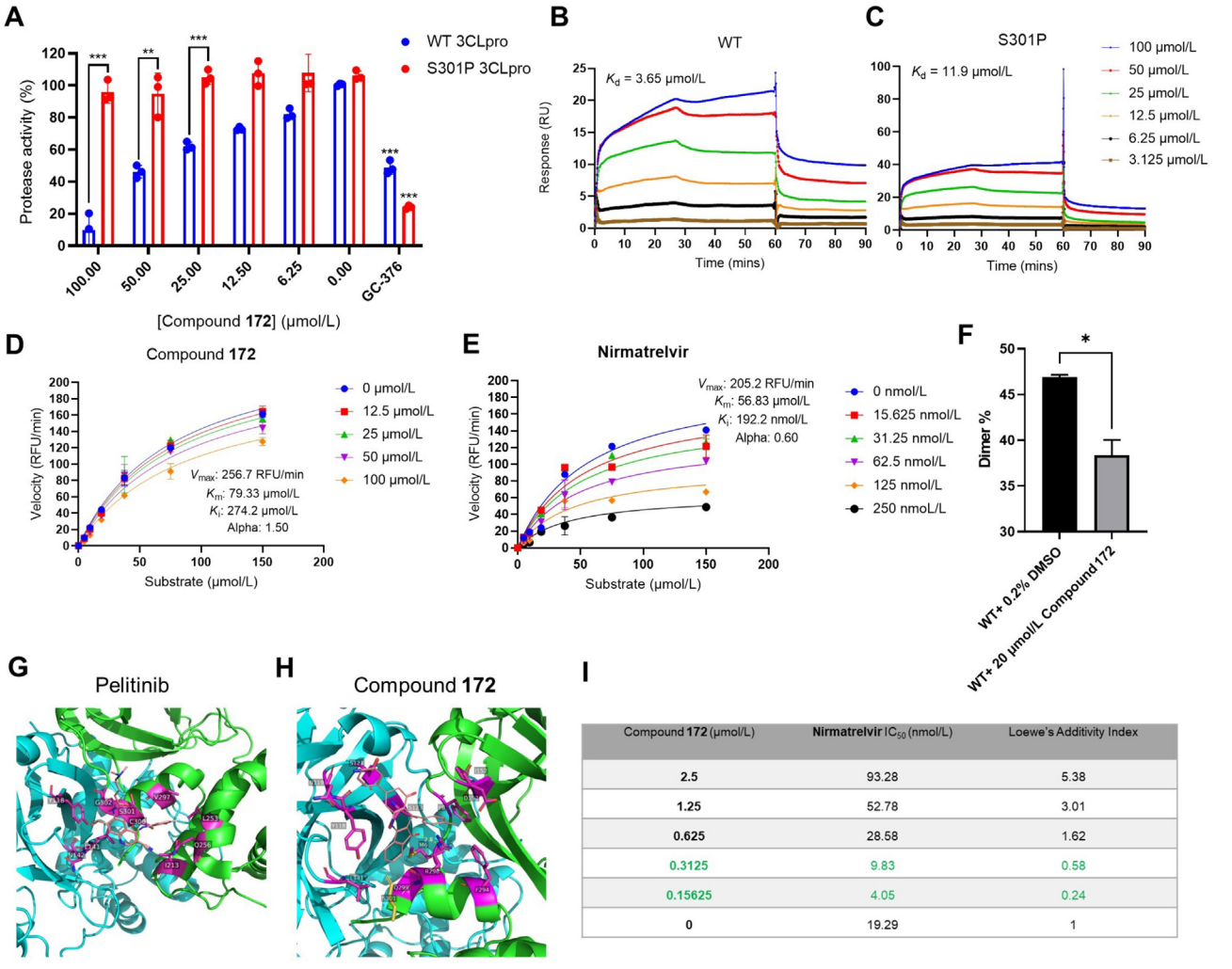

I

Compound **172** (μmol/L)	**Nirmatrelvir** IC_{50} (nmol/L)	Loewe's Additivity Index
2.5	93.28	5.38
1.25	52.78	3.01
0.625	28.58	1.62
0.3125	9.83	0.58
0.15625	4.05	0.24
0	19.29	1

Figure 4 Mechanistic investigation of compound **172.** (A) FRET-based protease activity assay. Recombinant WT and S301P 3CLpro were expressed and purified. Compound **172** was diluted from 100 to 6.26 μmol/L and incubated with 1.25 μmol/L WT or S301P 3CLpro at RT for 30 min. 50 μmol/L fluorophore-conjugated substrate was added to the mixture after 20 min as previously established. 200 nmol/L GC376 was added as a positive control. Both experiments were performed in triplicate. Statistical analysis by Student's *t*-test: Data present as mean ± SD. $^{***}P < 0.001$; $^{**}P < 0.01$; $^{*}P < 0.05$. (B, C) Surface plasmon resonance (SPR) spectroscopy of compound **172** with WT and S301P 3CLpro. The Biacore T-200 machine was used to conduct SPR spectroscopy. 40 μg/mL of protease was immobilized on a Series S Sensor Chip CM5. Compound **172** was added to the chip at gradient concentrations ranging from 100 to 3.125 μmol/L. Cytiva software was used to generate the association-dissociation graph and the dissociation constant (K_D). (D, E) Michaelis−Menton inhibition kinetics of compound **172** and Nirmatrelvir. 1.25 μmol/L WT 3CLpro was incubated with compound **172** or Nirmatrelvir in a gradient of concentrations at RT for 30 min, followed by the addition of fluorophore-conjugated substrate in a range of concentrations and measured in fluorescence (Excitation: 365 nm, Emission: 500−550 nm) in 20 min as initial velocity. (F) Analytical ultracentrifugation (AUC) for WT 3CLpro with compound **172**. 600 μg/mL WT 3CLpro was incubated with 20 μmol/L compound **172** or 0.2% DMSO before this sedimentation velocity experiment. The main peaks for 3CLpro monomer and dimer showed a sedimentation coefficient of 3.3 and 4.6 S respectively. Two independent experiments were performed. Statistical analysis by Student's *t*-test: Data are presented as mean ± SD. $^{***}P < 0.001$; $^{**}P < 0.01$; $^{*}P < 0.05$. (G, H) Intermolecular interaction of pelitinib and compound **172** to 3CLpro. Monomers are shown in cyan and green cartoon representations, respectively. Interacting residues of 3CLpro within 3.5 Å of compound are shown in magenta sticks and labelled accordingly. (I) List of Loewe's additivity (LA) indices calculated with the IC_{50} values of each compound combination. LA < 1, synergism; LA = 1, independent; LA > 1, antagonism. **172** concentrations that lowered Nirmatrelvir IC_{50} are highlighted in green. This experiment was conducted in triplicates.

coronavirus 3CLpro alignment analysis showed that M6, Y118, and Q299 are fully conserved amino acid residues, while N119 and L141 are highly similar residues among human coronaviruses, which explains compound **172** broad spectrum activity (Supporting Information Fig. S8). Furthermore, 10ns molecular dynamics (MD) simulation showed the binding of compound **172** was thermodynamically stable, with an average root mean square deviation (RMSD) value of 2 Å (Fig. S7B).

*3.4. In vivo antiviral activity and drug-likeness of compound **172***

Next, we evaluated the drug-likeness of compound **172**. To explore the potential off-target effect, safety panel assays focusing on 44 selected host targets including 24 GPCRs, 8 ion channels, 7 enzymes, 3 monoamine transporters, and 2 nuclear hormone receptors were evaluated. The result suggests that compound **172**

A

Name	Mean P_{app} (10^{-6} cm/s)		Efflux Ratio	Human Liver Microsome (HLM)	Mouse liver microsome (MLM)
	A to B	B to A		$T_{1/2}$ (min)	$T_{1/2}$ (min)
Compound **172**	1.423	1.797	1.26	33	35

B

Mouse ID	Animal Body Weight (g)	PK parameters									
		C_{max} (ng/mL)	T_{max} (h)	$T_{1/2}$ (h)	T_{last} (h)	$AUC_{0\text{-}last}$ (ng.h/mL)	$AUC_{0\text{-}inf}$ (ng.h/mL)	$MRT_{0\text{-}last}$ (h)	$MRT_{0\text{-}inf}$ (h)	AUC_{Extra} (%)	$AUMC_{Extra}$ (%)
M01	24.17	3219	0.250	0.749	8.00	3358	3361	0.949	0.956	0.0865	0.822
M02	22.18	2659	0.500	1.20	8.00	2959	2964	0.985	1.00	0.172	1.67
M03	22.34	2749	0.250	0.596	6.00	2809	2814	0.860	0.870	0.162	1.27
Mean	22.90	**2876**	**0.333**	**0.848**	**ND**	**3042**	**3046**	**0.931**	**0.942**	**0.140**	**1.25**
±SD	--	301	0.144	0.314	--	284	283	0.0643	0.0661	0.0467	0.424
CV (%)	--	10.5	43.3	37.0	--	9.33	9.28	6.91	7.02	33.3	33.8

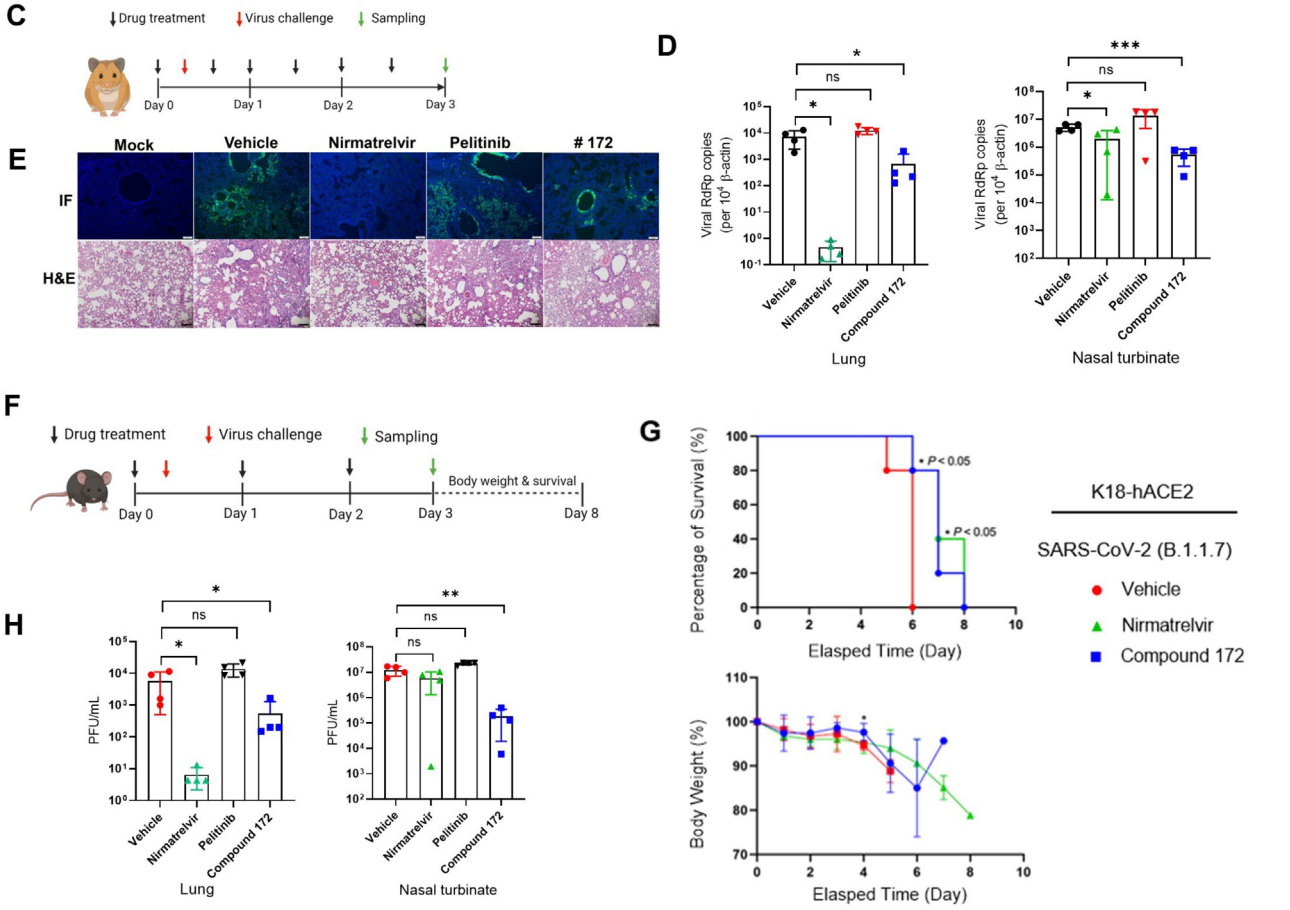

Figure 5 *In vivo* activity of compound **172.** (A) Permeability of compound **172** in Caco-2 cells and metabolic stability of **172** in mouse and human Liver microsomes. (B) *In vivo* pharmacokinetic profiling of compound **172** in a BALB/c mouse model ($n = 3$). (C) Schematics of compound **172** administration in a golden Syrian hamster model. Two groups of hamsters ($n = 4$) were given intranasal inoculations of 1000 PFU/animal of WT SARS-CoV-2. The treatment group ($n = 4$) received compound **172** (1 mg/kg) or nirmatrelvir (200 mg/kg) *via* intraperitoneal (ip) injection, or pelitinib (10 mg/kg) *via* oral gavage. The vehicle group ($n = 4$) was given 5% DMSO in 20% SBE-β-CD/0.9% saline. On the third day following the infection, the hamsters were euthanized for both viral yield and histopathological examination. (D) Hamsters lung and nasal turbinate viral yield were determined by RT-qPCR. Statistical analysis by one-way ANOVA: Data present as mean ± SD. $^{***}P < 0.001$; $^{**}P < 0.01$; $^{*}P < 0.05$. (E) Representative images of H&E-stained and IF-stained lung tissue sections from hamster treated as indicated. Scale bars: 100 μm. (F) Schematic of compound **172** administration in a K18-hACE2 mouse model. K18-hACE2 mice were intranasally inoculated with either Alpha (B.1.1.7, $n = 5$ for survival rate) or Omicron (BA.5, $n = 4$ for viral load detection) at 200 PFU/animal or 10,000 PFU/animal, respectively. The treatment group was given compound **172** (50 mg/kg) dissolved in a solution of 20% SBE-β-CD/0.9% saline, administered once daily *via* i.p. injection. The vehicle group was given 5% DMSO in 20% SBE-β-CD/0.9% saline using the same treatment regimen. The positive control group was given Nirmatrelvir (200 mg/kg) dissolved in a solution of 20% SBE-β-CD and 0.9% saline using the same treatment regimen. The mice in the survival study were monitored daily, and drugs were administered until they reached the humane endpoint or died. The mice in the viral load study were euthanized on the third day after the infection, and their lungs and nasal turbinate were collected for viral load quantification. (G) Mouse survival rate (upper panel) and daily body weight changes (lower panel) of K18-hACE2 mice. The comparison of survival rates between groups were analysed using Log-rank (Mantel−Cox) tests and that of body weight using two-way ANOVA. (H) K18-hACE2 mouse lung and nasal turbinate viral titer determined by standard plaque assay. Statistical analysis by one-way ANOVA: Data are presented as mean ± SD. $^{***}P < 0.001$; $^{**}P < 0.01$; $^{*}P < 0.05$; ns indicates not significant.

(10 μmol/L) showed no significant off-target effects on these host proteins (Supporting Information Table S1). Compound **172** exhibits moderate permeability and metabolic stability in cell cultures (Fig. 5A), and relatively good PK parameters in a BALB/c mouse model (Fig. 5B). The C_{max} of the compound is 6.89 μmol/L, which is around 3.8-fold higher than its antiviral

IC_{50} of 1.82 μmol/L. These results warrant further evaluation of compound **172**'s *in vivo* antiviral potency.

To evaluate the preclinical potential of compound **172**, it was tested in both golden Syrian hamster and K18-hACE20 mouse models. To investigate the antiviral activity of compound **172** in Golden Syrian hamster, the hamsters ($n = 4$) were infected with 1000 PFU WT SARS-CoV-2 virus and treated with 1 mg/kg compound **172** (treatment) or Vehicle (control) or Nirmatrelvir (200 mg/kg) by intraperitoneal (i.p.) injection or Pelitinib (oral 10 mg/kg) at 12-h intervals (Fig. 5C). Notably, the lung and nasal turbinate (NT) of the hamsters in the **172**-treated group exhibited a 1-log10 reduction when compared to the control group (Fig. 5D). The protection by Nirmatrelvir is extraordinarily potent in animal lungs with >4-log10 reduction, whereas that from Pelitinib is marginal (Fig. 5D). Histopathological and IF staining of the lungs of the **172**-treated group also showed a lower degree of lymphocyte infiltration and reduced SARS-CoV-2 N antigen expression when compared to the control group (Fig. 5E).

On the other hand, compound **172** was also tested in the K18-hACE2 transgenic mice model. For the survival study, K18-hACE2 transgenic mice ($n = 5$) were challenged with 200 PFU SARS-CoV-2 Alpha variant (B.1.1.7) and treated with either 50 mg/kg compound **172** (treatment), 5% DMSO in vehicle (vehicle control), or 200 mg/kg Nirmatrelvir (positive control), by i.p. injection once daily, until death or reaching the humane endpoint (Fig. 5F). A higher drug dosage of **172** was administered due to the high susceptibility of K18-hACE2 mice to Alpha SARS-CoV-2 infection. i.p. injection was utilized to enhance the systemic dissemination of both compound **172** and Nirmatrelvir. In the vehicle control group, one mouse died on Day 5, and all remaining mice died on Day 6 (Fig. 5G). However, in the **172** treated groups, a delayed time of death was observed as one mouse died on Day 6, and all remaining mice died on Day 7 and/or 8 (Fig. 5G). The same delay in death was observed in the Nirmatrelvir group, where one mouse died on Day 6, and all remaining mice died on Day 8 (Fig. 5G). The mice's body weight was monitored daily, and a significant benefit in weight percentage was observed between the **172** and the vehicle control group on Day 4 (Fig. 5G). For the viral load study, K18-hACE2 transgenic mice were infected with 10,000 PFU Omicron BA.5 variant. In line with the finding in hamsters, compound **172** can reduce live virus titer in both the upper and lower respiratory tract of infected mice (Fig. 5H). Taken together, these findings suggest that compound **172** is effective against SARS-CoV-2 infection *in vivo*.

4. Discussion

In this study, we systematically screened a SMART™ chemical library with 50,213 small molecules against live SARS-CoV-2 infection and identified a 3CLpro-targeting inhibitor compound **172** with reasonably good selectivity, broad-coronavirus coverage and antiviral activity *in vivo*. Compound **172** binds to the domain III of 3CLpro, which is likely to interfere with protein dimerization, thus destabilizing protein conformation. Compound **172** exhibits drug synergism with Nirmatrelvir at nanomolar concentrations, which reduces the likelihood of antiviral resistance. Importantly, the pan-coronavirus and *in vivo* antiviral property signifies the clinical potential of compound **172**.

The SARS-CoV-2 3CLpro is also known as Main Protease, which plays a crucial role in processing the viral polyprotein during early replication by cleaving at specific sequences between NSP5-16[9,49,50]. The 3CLpro is conserved among coronaviruses and functions as a dimer with three domains[9]. Domains I (residues 10−99) and II (residues 100−182) are homologues of the 3C protease of Picornaviruses, due to similar secondary structures[9,51]. The catalytic dyads (C145 and H41) are situated within Domains I and II[9]. However, domain III (residues 198−303) is uniquely found in coronavirus and is involved in the dimerization of the protease[9,52−55]. Since the **172**-resistant S301P mutation in the 3CLpro is within domain III, the compound is likely to interfere with 3CLpro dimerization. Our AUC assay directly demonstrated that the compound **172** can disrupt the 3CLpro dimerization, inducing considerable changes on 3CLpro secondary structures (Fig. 4F). Furthermore, the 3CLpro S301P mutant only conferred resistance towards compound **172** but not Nirmatrelvir (Fig. 3D). These results suggested that compound **172** inhibits the 3CLpro *via* a distinct mechanism from Nirmatrelvir.

The association of S301 with an allosteric site on 3CLpro has been reported in a previous X-ray crystallography screening[48]. One of the screened compounds, Pelitinib, was predicted to interact with the S301 and bind to an allosteric site situated between the 3CLpro monomers[48]. Notably, Pelitinib exhibited a dose-dependent inhibition of WT virus replication but not the mutant virus. This confirms that the S301 residue is essential for Pelitinib's antiviral activity. Compared with **172**, however, Pelitinib showed considerable high cytotoxicity and off-target effects as a repurposed anticancer treatment. Molecular docking predicted that compound **172** binds to an allosteric site different from Pelitinib (Fig. 4G and H). The C-terminal sequence of 3CLpro forms an alpha helix (Fig. 4H). Since proline is known to destabilize alpha helix structure[56], S301P could alter the secondary structure of the C-terminal sequences, thus disrupting the binding pocket of **172**. Several previous studies have reported that substrate-binding is a crucial factor for 3CLpro dimerization[57−60], inducing the opposite effect of compound **172**. Therefore, there is a negative feedback relationship between substrate-binding and **172**-binding, which explains the low competitiveness of compound **172**. Taken together, these findings indicate compound **172** inhibits 3CLpro *via* disrupting 3CLpro dimerization, by binding to a novel allosteric site associated with S301. Three out of five fully conserved and two out of five highly similar amino acids are found within the **172** binding pocket (Fig. S8), which explains the pan-coronavirus activity of the compound. Lastly, the monomeric form of 3CLpro was expressed and purified for affinity assay. Compound **172** was discovered to have 46-fold higher affinity towards the monomer, further validating **172** binding to the dimeric interface of 3CLpro (Fig. S6B).

There are limitations in this study. Firstly, only one concentration was measured for CPE inhibition of each compound in SMART™ library, which may overlook compounds with antiviral activity at higher concentrations than 5 μmol/L. Secondly, primary screening was performed on VeroE6, which may miss human-specific compounds. In general, a small molecule should follow the Lipinski's Rule of Five with a suitable adsorption/distribution/metabolism/excretion (ADME) profile to be effective *in vivo*. Although compound **172** was effective against multiple coronaviruses *in vitro*, its antiviral activity was not as potent, likely due to its unoptimized structure for *in vivo* application. The high hydrophobicity of compound **172** may pose challenges in drug absorption and increase the likelihood of bioaccumulation in fat tissue. Therefore, the structure of compound **172** should be

ADME-optimized to fully unlock its clinical potential. To fully understand the mechanism of compound **172** binding with 3CLpro, X-ray crystallography or Cryo-electron microscopy is recommended for follow-up study. Nevertheless, our work facilitates the design of novel antivirals for emerging coronaviruses and the primary screening data would be shared in the public domain for artificial intelligence training.

5. Conclusions

Compound **172** is an allosteric inhibitor that targets the 3CLpro dimerization domain with pan-coronavirus antiviral activity. Notably, it exhibited *in vivo* antiviral activity and drug synergism with Nirmatrelvir, which could lower the risk of antiviral resistance.

Acknowledgments

This study was partly supported by National Natural Science Foundation of China (NSFC)/Research Grants Council (RGC) Joint Research Scheme (N_HKU767/22 and 82261160398); Health and Medical Research Fund (COVID190121), the Food and Health Bureau, The Government of the Hong Kong Special Administrative Region; the National Natural Science Foundation of China (32322087, 32300134, and 82272337); Guangdong Natural Science Foundation (2023A1515012907); Health@InnoHK, Innovation and Technology Commission, the Government of the Hong Kong Special Administrative Region; the Collaborative Research Fund (C7060-21G and C7002-23Y) and Theme-Based Research Scheme (T11-709/21-N) of the Research Grants Council, The Government of the Hong Kong Special Administrative Region; Partnership Programme of Enhancing Laboratory Surveillance and Investigation of Emerging Infectious Diseases and Antimicrobial Resistance for the Department of Health of the Hong Kong Special Administrative Region Government; Sanming Project of Medicine in Shenzhen, China (SZSM201911014); the High Level-Hospital Program, Health Commission of Guangdong Province, China; the research project of Hainan Academician Innovation Platform (YSPTZX202004); Emergency Collaborative Project of Guangzhou Laboratory (EKPG22-01); and the National Key R&D Program of China (projects 2021YFC0866100 and 2023YFC3041600); The University of Hong Kong Seed Fund for Collaborative Research (2207101537); and Hunan University (521119400156), and donations of Providence Foundation Limited (in memory of the late Lui Hac Minh). The funding sources had no role in the study design, data collection, analysis, interpretation, or writing of the report.

Author contributions

Chris Chun-Yiu Chan: Data curation, Formal analysis, Investigation, Methodology, Visualization, Writing − original draft, Writing − review & editing. Qian Guo: Data curation, Formal analysis, Investigation, Methodology, Visualization, Writing − review & editing. Jasper Fuk-Woo Chan: Formal analysis, Funding acquisition, Methodology, Resources, Supervision. Kaiming Tang: Investigation. Jian-Piao Cai: Investigation. Kenn Ka-Heng Chik: Investigation. Yixin Huang: Investigation. Mei Dai: Methodology. Bo Qin: Methodology. Chon Phin Ong: Investigation, Visualization. Allen Wing-Ho Chu: Investigation. Wan-Mui Chan: Investigation. Jonathan Daniel Ip: Investigation. Lei Wen: Investigation, Visualization. Jessica Oi-Ling Tsang: Investigation. Tong-Yun Wang: Investigation. Yubin Xie: Investigation. Zhenzhi Qin: Investigation. Jianli Cao: Investigation. Zi-Wei Ye: Investigation. Hin Chu: Resources, Supervision. Kelvin Kai-Wang To: Resources, Supervision. Xing-Yi Ge: Resources. Tao Ni: Resources, Supervision. Dong-Yan Jin: Resources, Supervision. Sheng Cui: Funding acquisition, Supervision. Kwok-Yung Yuen: Funding acquisition, Resources, Supervision. Shuofeng Yuan: Conceptualization, Formal analysis, Funding acquisition, Methodology, Resources, Supervision, Writing − original draft, Writing − review & editing.

Conflicts of interest

The authors have no conflict to declare.

Appendix A. Supporting information

Supporting information to this article can be found online at https://doi.org/10.1016/j.apsb.2024.05.026.

References

1. Peiris JS, Lai ST, Poon LL, Guan Y, Yam LY, Lim W, et al. Coronavirus as a possible cause of severe acute respiratory syndrome. *Lancet* 2003;**361**:1319−25.
2. Zaki AM, van Boheemen S, Bestebroer TM, Osterhaus AD, Fouchier RA. Isolation of a novel coronavirus from a man with pneumonia in Saudi Arabia. *N Engl J Med* 2012;**367**:1814−20.
3. Zhou P, Yang XL, Wang XG, Hu B, Zhang L, Zhang W, et al. A pneumonia outbreak associated with a new coronavirus of probable bat origin. *Nature* 2020;**579**:270−3.
4. Chan JF, Yuan S, Kok KH, To KK, Chu H, Yang J, et al. A familial cluster of pneumonia associated with the 2019 novel coronavirus indicating person-to-person transmission: a study of a family cluster. *Lancet* 2020;**395**:514−23.
5. Guan WJ, Ni ZY, Hu Y, Liang WH, Ou CQ, He JX, et al. Clinical characteristics of coronavirus disease 2019 in China. *N Engl J Med* 2020;**382**:1708−20.
6. Chen N, Zhou M, Dong X, Qu J, Gong F, Han Y, et al. Epidemiological and clinical characteristics of 99 cases of 2019 novel coronavirus pneumonia in Wuhan, China: a descriptive study. *Lancet* 2020;**395**:507−13.
7. Huang C, Wang Y, Li X, Ren L, Zhao J, Hu Y, et al. Clinical features of patients infected with 2019 novel coronavirus in Wuhan, China. *Lancet* 2020;**395**:497−506.
8. Menni C, Valdes AM, Polidori L, Antonelli M, Penamakuri S, Nogal A, et al. Symptom prevalence, duration, and risk of hospital admission in individuals infected with SARS-CoV-2 during periods of omicron and delta variant dominance: a prospective observational study from the ZOE COVID Study. *Lancet* 2022;**399**:1618−24.
9. Zhang L, Lin D, Sun X, Curth U, Drosten C, Sauerhering L, et al. Crystal structure of SARS-CoV-2 main protease provides a basis for design of improved α-ketoamide inhibitors. *Science* 2020;**368**:409−12.
10. Owen DR, Allerton CMN, Anderson AS, Aschenbrenner L, Avery M, Berritt S, et al. An oral SARS-CoV-2 M^{pro} inhibitor clinical candidate for the treatment of COVID-19. *Science* 2021;**374**:1586−93.
11. Gao Y, Yan L, Huang Y, Liu F, Zhao Y, Cao L, et al. Structure of the RNA-dependent RNA polymerase from COVID-19 virus. *Science* 2020;**368**:779−82.
12. Liu L, Iketani S, Guo Y, Chan JFW, Wang M, Liu L, et al. Striking antibody evasion manifested by the Omicron variant of SARS-CoV-2. *Nature* 2022;**602**:676−81.

13. Gordon CJ, Tchesnokov EP, Woolner E, Perry JK, Feng JY, Porter DP, et al. Remdesivir is a direct-acting antiviral that inhibits RNA-dependent RNA polymerase from severe acute respiratory syndrome coronavirus 2 with high potency. *J Biol Chem* 2020;**295**:6785−97.
14. Gordon CJ, Tchesnokov EP, Schinazi RF, Götte M. Molnupiravir promotes SARS-CoV-2 mutagenesis *via* the RNA template. *J Biol Chem* 2021;**297**:100770.
15. Mukae H, Yotsuyanagi H, Ohmagari N, Doi Y, Sakaguchi H, Sonoyama T, et al. Efficacy and safety of ensitrelvir in patients with mild-to-moderate coronavirus disease 2019: the phase 2b part of a randomized, placebo-controlled, phase 2/3 study. *Clin Infect Dis* 2022;**76**:1403−11.
16. Beigel JH, Tomashek KM, Dodd LE, Mehta AK, Zingman BS, Kalil AC, et al. Remdesivir for the treatment of Covid-19—final report. *N Engl J Med* 2020;**383**:1813−26.
17. Jayk Bernal A, Gomes da Silva MM, Musungaie DB, Kovalchuk E, Gonzalez A, Delos Reyes V, et al. Molnupiravir for oral treatment of Covid-19 in nonhospitalized patients. *N Engl J Med* 2022;**386**:509−20.
18. Xie Y, Yin W, Zhang Y, Shang W, Wang Z, Luan X, et al. Design and development of an oral remdesivir derivative VV116 against SARS-CoV-2. *Cell Res* 2021;**31**:1212−4.
19. Zhang JL, Li YH, Wang LL, Liu HQ, Lu SY, Liu Y, et al. Azvudine is a thymus-homing anti-SARS-CoV-2 drug effective in treating COVID-19 patients. *Signal Transduct Target Ther* 2021;**6**:414.
20. Merches K, Breunig L, Fender J, Brand T, Batz V, Idel S, et al. The potential of remdesivir to affect function, metabolism and proliferation of cardiac and kidney cells *in vitro*. *Arch Toxicol* 2022;**96**:2341−60.
21. Zhou S, Hill CS, Sarkar S, Tse LV, Woodburn BMD, Schinazi RF, et al. Beta-D-*N*4-hydroxycytidine inhibits SARS-CoV-2 through lethal mutagenesis but is also mutagenic to mammalian cells. *J Infect Dis* 2021;**224**:415−9.
22. Unoh Y, Uehara S, Nakahara K, Nobori H, Yamatsu Y, Yamamoto S, et al. Discovery of S-217622, a noncovalent oral SARS-CoV-2 3CL protease inhibitor clinical candidate for treating COVID-19. *J Med Chem* 2022;**65**:6499−512.
23. Zhan Y, Lin Z, Liang J, Sun R, Li Y, Lin B, et al. Leritrelvir for the treatment of mild or moderate COVID-19 without co-administered ritonavir: a multicentre randomised, double-blind, placebo-controlled phase 3 trial. *EClinicalMedicine* 2024;**67**:102359.
24. Wang F, Xiao W, Tang Y, Cao M, Shu D, Asakawa T, et al. Efficacy and safety of SIM0417 (SSD8432) plus ritonavir for COVID-19 treatment: a randomised, double-blind, placebo-controlled, phase 1b trial. *Lancet Reg Health West Pac* 2023;**38**:100835.
25. Hu Y, Lewandowski EM, Tan H, Zhang X, Morgan RT, Zhang X, et al. Naturally occurring mutations of SARS-CoV-2 main protease confer drug resistance to nirmatrelvir. *ACS Cent Sci* 2023;**9**:1658−69.
26. Stevens LJ, Pruijssers AJ, Lee HW, Gordon CJ, Tchesnokov EP, Gribble J, et al. Mutations in the SARS-CoV-2 RNA-dependent RNA polymerase confer resistance to remdesivir by distinct mechanisms. *Sci Transl Med* 2022;**14**:eabo0718.
27. Iketani S, Mohri H, Culbertson B, Hong SJ, Duan Y, Luck MI, et al. Multiple pathways for SARS-CoV-2 resistance to nirmatrelvir. *Nature* 2023;**613**:558−64.
28. Kiso M, Furusawa Y, Uraki R, Imai M, Yamayoshi S, Kawaoka Y. *In vitro* and *in vivo* characterization of SARS-CoV-2 strains resistant to nirmatrelvir. *Nat Commun* 2023;**14**:3952.
29. Choi H, Kim JY, Chang YT, Nam HG. Forward chemical genetic screening. *Methods Mol Biol* 2014;**1062**:393−404.
30. Cong F, Cheung AK, Huang SM. Chemical genetics-based target identification in drug discovery. *Annu Rev Pharmacol Toxicol* 2012;**52**:57−78.
31. Zhao Y, Fang C, Zhang Q, Zhang R, Zhao X, Duan Y, et al. Crystal structure of SARS-CoV-2 main protease in complex with protease inhibitor PF-07321332. *Protein Cell* 2022;**13**:689−93.
32. Yuan S, Yin X, Meng X, Chan JF, Ye ZW, Riva L, et al. Clofazimine broadly inhibits coronaviruses including SARS-CoV-2. *Nature* 2021;**593**:418−23.
33. Yuan S, Chu H, Huang J, Zhao X, Ye ZW, Lai PM, et al. Viruses harness YxxØ motif to interact with host AP2M1 for replication: a vulnerable broad-spectrum antiviral target. *Sci Adv* 2020;**6**:eaba7910.
34. Lewandowski K, Xu Y, Pullan ST, Lumley SF, Foster D, Sanderson N, et al. Metagenomic nanopore sequencing of influenza virus direct from clinical respiratory samples. *J Clin Microbiol* 2019;**58**:e00963-19.
35. Artic network-nCoV 2019 sequencing protocol. Available from: https://artic.network/ncov-2019 (Accessed 26/3).
36. Liang R, Ye ZW, Ong CP, Qin Z, Xie Y, Fan Y, et al. The spike receptor-binding motif G496S substitution determines the replication fitness of SARS-CoV-2 Omicron sublineage. *Emerg Microbes Infect* 2022;**11**:2093−101.
37. Yuan S, Chu H, Chan JF, Ye ZW, Wen L, Yan B, et al. SREBP-dependent lipidomic reprogramming as a broad-spectrum antiviral target. *Nat Commun* 2019;**10**:120.
38. Copeland RA. *Evaluation of enzyme inhibitors in drug discovery: a guide for medicinal chemists and pharmacologists.*. John Wiley & Sons; 2013.
39. Kim S, Chen J, Cheng T, Gindulyte A, He J, He S, et al. PubChem 2023 update. *Nucleic Acids Res* 2023;**51**:D1373−80.
40. Berman HM, Westbrook J, Feng Z, Gilliland G, Bhat TN, Weissig H, et al. The protein data bank. *Nucleic Acids Res* 2000;**28**:235−42.
41. Gordon JC, Myers JB, Folta T, Shoja V, Heath LS, Onufriev A. H++: a server for estimating p*K*a s and adding missing hydrogens to macromolecules. *Nucleic Acids Res* 2005;**33**:W368−71.
42. MetaPocket: a meta approach to improve protein ligand binding site prediction. *OMICS* 2009;**13**:325−30.
43. Stroganov OV, Novikov FN, Stroylov VS, Kulkov V, Chilov GG. Lead finder: an approach to improve accuracy of protein−ligand docking, binding energy estimation, and virtual screening. *J Chem Inf Model* 2008;**48**:2371−85.
44. Maier JA, Martinez C, Kasavajhala K, Wickstrom L, Hauser KE, Simmerling C. ff14SB: improving the accuracy of protein side chain and backbone parameters from ff99SB. *J Chem Theory Comput* 2015;**11**:3696−713.
45. Wang J, Wolf RM, Caldwell JW, Kollman PA, Case DA. Development and testing of a general amber force field. *J Comput Chem* 2004;**25**:1157−74.
46. Case DA, Cheatham 3rd TE, Darden T, Gohlke H, Luo R, Merz Jr KM, et al. The amber biomolecular simulation programs. *J Comput Chem* 2005;**26**:1668−88.
47. Yoshimura N, Kudoh S, Kimura T, Mitsuoka S, Matsuura K, Hirata K, et al. EKB-569, a new irreversible epidermal growth factor receptor tyrosine kinase inhibitor, with clinical activity in patients with non-small cell lung cancer with acquired resistance to gefitinib. *Lung Cancer* 2006;**51**:363−8.
48. Günther S, Reinke PYA, Fernández-García Y, Lieske J, Lane TJ, Ginn HM, et al. X-ray screening identifies active site and allosteric inhibitors of SARS-CoV-2 main protease. *Science* 2021;**372**:642−6.
49. Chan JF, Kok KH, Zhu Z, Chu H, To KK, Yuan S, et al. Genomic characterization of the 2019 novel human-pathogenic coronavirus isolated from a patient with atypical pneumonia after visiting Wuhan. *Emerg Microbes Infect* 2020;**9**:221−36.
50. Hoffman RL, Kania RS, Brothers MA, Davies JF, Ferre RA, Gajiwala KS, et al. Discovery of ketone-based covalent inhibitors of coronavirus 3CL proteases for the potential therapeutic treatment of COVID-19. *J Med Chem* 2020;**63**:12725−47.
51. Gorbalenya AE, Donchenko AP, Blinov VM, Koonin EV. Cysteine proteases of positive strand RNA viruses and chymotrypsin-like serine proteases: a distinct protein superfamily with a common structural fold. *FEBS Lett* 1989;**243**:103−14.
52. Chou CY, Chang HC, Hsu WC, Lin TZ, Lin CH, Chang GG. Quaternary structure of the severe acute respiratory syndrome (SARS) coronavirus main protease. *Biochemistry* 2004;**43**:14958−70.
53. Hsu WC, Chang HC, Chou CY, Tsai PJ, Lin PI, Chang GG. Critical assessment of important regions in the subunit association and

catalytic action of the severe acute respiratory syndrome coronavirus main protease. *J Biol Chem* 2005;**280**:22741−8.
54. Tan J, Verschueren KH, Anand K, Shen J, Yang M, Xu Y, et al. pH-dependent conformational flexibility of the SARS-CoV main proteinase (M^{pro}) dimer: molecular dynamics simulations and multiple X-ray structure analyses. *J Mol Biol* 2005;**354**:25−40.
55. Shi J, Sivaraman J, Song J. Mechanism for controlling the dimer-monomer switch and coupling dimerization to catalysis of the severe acute respiratory syndrome coronavirus 3C-like protease. *J Virol* 2008;**82**:4620−9.
56. Nilsson I, Sääf A, Whitley P, Gafvelin G, Waller C, von Heijne G. Proline-induced disruption of a transmembrane alpha-helix in its natural environment. *J Mol Biol* 1998;**284**:1165−75.
57. Noske GD, Song Y, Fernandes RS, Chalk R, Elmassoudi H, Koekemoer L, et al. An in-solution snapshot of SARS-CoV-2 main protease maturation process and inhibition. *Nat Commun* 2023;**14**:1545.
58. Ferreira GM, Kronenberger T, Tonduru AK, Hirata RDC, Hirata MH, Poso A. SARS-CoV-2 M^{pro} conformational changes induced by covalently bound ligands. *J Biomol Struct Dyn* 2022;**40**:12347−57.
59. Li C, Qi Y, Teng X, Yang Z, Wei P, Zhang C, et al. Maturation mechanism of severe acute respiratory syndrome (SARS) coronavirus 3C-like proteinase. *J Biol Chem* 2010;**285**:28134−40.
60. Cheng SC, Chang GG, Chou CY. Mutation of Glu-166 blocks the substrate-induced dimerization of SARS coronavirus main protease. *Biophys J* 2010;**98**:1327−36.